Lagrangian study of the Panama Bight and surrounding regions

Alexis Chaigneau,[1,2] Rodrigo Abarca del Rio,[3] and François Colas[4,5]

Received 8 February 2006; revised 3 May 2006; accepted 31 May 2006; published 13 September 2006.

[1] Near-surface circulation of the Panama Bight and surrounding regions [0–9°N; 73°W–90°W] was studied using satellite-tracked drifter trajectories from 1979–2004. This region encompasses three major currents showing typical velocities of ~30 cm s^{-1}: (1) the eastward North Equatorial Counter Current (NECC), (2) the near-circular Panama Bight Cyclonic Gyre (PBCG), and (3) the westward South Equatorial Current (SEC). We do not observe significant modification of the mean surface circulation during El Niño Southern Oscillation events, even if the SEC is slightly reinforced during relatively warm El Niño periods. At seasonal scales, the circulation is strongly controlled by the activity of the Panama wind-jet: in boreal winter, the currents are stronger and an anticyclonic cell is present west of the PBCG. This dipole leads to a strong ~200 km wide southward current which then disappears during the rest of the year. In summer, the three major currents have reduced intensity by 30%–40%. Large-scale current vorticity shows that the upwelling associated with the PBCG is also 3–4 times stronger in winter than during summer months. The kinetic energy is largely dominated by eddy activity and its intensity is double in winter than during summer. Ageostrophic motions and eddy activity appear to have a substantial impact on the energy spatial distribution. In the NECC and SEC regions, Lagrangian scales are anisotropic and zonally enhanced in the direction of the mean currents. The typical integral time and length scales of these regions are 2.5 days and 50–60 km in the zonal direction and 1.5 days and 25–30 km in the meridional direction. Lateral eddy diffusivity coefficients are on the order of 11–14 10^7 cm^2 s^{-1} zonally and 5–6 10^7 cm^2 s^{-1} meridionally. In contrast, in the PBCG region, the Lagrangian characteristics are isotropic with typical timescales of 1.7 days, space scales of 30 km and eddy diffusivity coefficients of 6 10^7 cm^2 s^{-1} in both directions.

Citation: Chaigneau, A., R. Abarca del Rio, and F. Colas (2006), Lagrangian study of the Panama Bight and surrounding regions, *J. Geophys. Res.*, *111*, C09013, doi:10.1029/2006JC003530.

1. Introduction

[2] In the Eastern Tropical Pacific (ETP) close to the Panama Bight, the ocean-atmosphere coupled system is strongly influenced by the topography of the Central American continent. The Central American Cordillera known as Sierra Madre, which on average reaches heights of around 1000 m, contains three low-elevation gaps (~300 m) located along the gulfs of Tehuantepec (southwest of Mexico, 20°N) [*McCreary et al.*, 1989], Papagayo (Nicaragua-Costa Rica boundary, 10°N) [*Trasviña et al.*, 1995], and the Panama Bight (Pacific Panama coast) [*Chelton et al.*, 2000a; *Chelton*, 2000]. They allow intense and relatively narrow wind-jets to blow from tropical Atlantic to tropical Pacific regions.

[3] These strong jets play an important role in the physical and biological properties of the ETP [*Xie et al.*, 2005; *Rodríguez-Rubio and Stuardo*, 2002] and lead to zonal variations of mechanical forcing and ocean properties as far west as 100°W–110°W [*Kessler*, 2006]. On both sides of the jets, the wind curl forces the predominantly zonal dynamics of the equatorial central Pacific to distort and to adopt a more complex three-dimensional structure in the ETP, inducing a significant vertical transport [*Kessler*, 2002].

[4] The ETP ocean circulation exhibits important temporal variations from intraseasonal to interannual timescales. At intraseasonal scales, the region is subject to the tropical dynamics of Kelvin, Rossby and instability waves [*Kessler and McPhaden*, 1995; *Chelton et al.*, 2000b; *Yu and Liu*, 2003; *Yuan*, 2005]. At seasonal timescales, surface currents in the Panama Bight respond principally to local wind forcing [*Rodríguez-Rubio et al.*, 2003], with intense northeast jets blowing offshore of the Gulf of Panama during winter and southeast trade winds blowing across the equator as far as 8°N in summer [*Fiedler*, 2002a]. The seasonal meridional shift of the intertropical convergence zone,

[1] IRD, IPSL-LOCEAN, UMR CNRS Université P. et M. Curie/IRD/MNHN, Paris, France.
[2] Also at Laboratorio de Procesos Oceanográficos y Clima (PROFC), Universidad de Concepción, Concepción, Chile.
[3] Departamento de Geofísica (DGEO), Universidad de Concepción, Concepción, Chile.
[4] Instituto del Mar de Peru (IMARPE), Lima, Peru.
[5] Now at Institute of Geophysics and Planetary Physics (IGPP), University of California, Los Angeles, Los Angeles, California, USA.

0148-0227/06/2006JC003530

which pilots the central Pacific circulation, has apparently less effect on the ocean dynamics east of 100°W [*Kessler*, 2006]. At interannual scales, this region is strongly influenced by El Niño Southern Oscillation (ENSO) events [*Fiedler*, 2002b], which can have dramatic impacts on the biogeochemistry [*Chavez et al.*, 1999]: by reducing the coastal ETP upwelling of cold, nutrient-rich water that sustains large fish populations, El Niño periods have a strong impact on the fishery and economy of the border countries.

[5] Aside from being a key region for local to world wide climate variations through atmospheric teleconnections [*Enfield*, 1996; *Enfield and Alfaro*, 1999; *Alfaro*, 2000; *Taylor et al.*, 2002], the ETP, including the Panama Bight and surrounding regions, plays a preponderant role in the control of ocean-atmosphere CO2 fluxes [*Tans et al.*, 1990; *Chavez et al.*, 1999] and can represent up to 20–50% of new production of the world ocean [*Loubere*, 2000]. Insight on the near-surface dynamics of this region may thus enhance knowledge of the coupling between physics and biogeochemistry, but also on the retroaction on climate through CO2 fluxes. Investigation of the ETP surface circulation characteristics and variability is also important given their large impact on different marine ecosystems [*Ballance et al.*, 1997; *Spear et al.*, 2001; *Fiedler*, 1999, 2002a] and on commercial fish stocks [*Fiedler*, 2002b].

[6] Despite the importance of the ETP surface circulation on different areas, few research works (to the best of our knowledge) have investigated its current characteristics after the 1960s [*Kessler*, 2006]. Considering more particularly the Panama Bight and surrounding regions, *Fiedler* [2002a] has briefly described the monthly surface circulation obtained from ship-drift records, while *Rodríguez-Rubio et al.* [2003] have studied the seasonal variations of the geostrophic currents in the Bight based on satellite altimetry data. More recently, *Kessler* [2006] proposed a review of the global ETP circulation which briefly described the Gulf of Panama. However, in this latter region, there is still a lack of details on the surface circulation and its variability, on the Lagrangian properties of the turbulent flow and some of its characteristics. These problematic are also important for the management of marine activities, considering that this area is an attractive area for tourism, fishing and commerce. Commercial navigation is particularly important given that the Panama Canal is one of the most highly traveled waterways in the world (~12 000 ships per year).

[7] In the present study, 25 years of satellite-tracked drifters data are investigated to examine some open questions related to the near-surface characteristics of the Panama Bight and surrounding regions. The paper is organized as follows. Section 2 provides a description of the data set and the methods used to compute the near-surface circulation. Section 3 deals with the large-scale surface currents and their spatio-temporal variability. In section 4 we investigate the near-surface kinematic properties. Section 5 analyzes the Lagrangian scales and lateral eddy diffusivity coefficients. Finally, the results are summarized in section 6.

2. Data and Methods

2.1. Surface Drifters Data Set

[8] The surface satellite-tracked drifters data set spans the period 1979–2004 and is part of the Global Drifter Program/Surface Velocity Program. A total of 250 drifters crossed the study region which extends over ~1.2 10^6 km^2 between 0° and 9°N and from the Central American coasts of Ecuador, Colombia and Panama to 90°W (Figure 1a). Of these 250 drifters, only 72 were deployed into the study region (black dots on Figure 1a). The mean lifetime of the drifters in the study region was 2 months, with a large variability ranging from a few days to around one year. In order to reduce surface drag induced by wind and waves, the drifters were equipped with a 7 m holey-sock drogue centered at a depth of 15 m and only data from buoys reporting attached drogues are used. The drifters were also equipped with a thermistor providing surface temperature measurements not used in this study. Readers interested in more details on the design of the drifters are referred to *Sybrandy and Niiler* [1991], *Niiler et al.* [1995], and *Niiler* [2001].

[9] The Lagrangian drifters data are estimated from Doppler measurements from the ARGOS satellite service and transmitted to the Atlantic Oceanographic and Meteorological Laboratory (AOML) in Miami USA. Drifter positions, irregularly distributed in time, are then quality controlled and interpolated to uniform 6 hour intervals by a "kriging" optimal interpolation procedure [*Hansen and Poulain*, 1996]. Velocity components are then calculated from these positions by a centered difference scheme. In the extra-equatorial regions, the data are often daily averaged to remove high frequency energy associated with tides and inertial currents [e.g., *Swenson and Niiler*, 1996; *Chaigneau and Pizarro*, 2005]. In the near-equatorial study region both the amplitude of the internal tides and the energy flux from wind to ocean inertial motions can be important [*Niwa and Hibiya*, 2001; *Ray and Egbert*, 2004; *Alford*, 2003; *Jiang et al.*, 2005]. However, we decided to analyze directly the 6h interval data distributed by the AOML, for the two following main reasons: firstly, results obtained from the 6h interval data and from daily averaged data were compared and did not show significant differences. This suggests that diurnal tides do not significantly affect drifter trajectories; this is also confirmed by the absence of a significant peak in the mean energy spectrum for the tidal frequency band. Secondly, in the study region inertial periods vary from around 3 days at 9°N to more than 15 days south of 2°N where Coriolis force vanishes and it is thus difficult to remove or filter out the inertial motions and keep the signals associated with mesoscale activity. In order to increase the number of observations, this study is thus based on more than 65 000 data uniformly interpolated at 6h intervals.

2.2. Spatio-Temporal Distribution of the Data

[10] The spaghetti diagram of drifter trajectories (Figure 1a) shows a relatively high concentration of observations in the whole study region, except in the southeast and northwest parts of the domain and along the Panama coast in the shallow area west of 81°W. Between 1979 and 2004, yearly distribution of the number of velocity observations (Figure 1b) shows that the region was irregularly sampled at interannual timescales. Less than 500 velocity data were observed in 1979 and 1981 and a maximum of around 9 000 and 11 000 observations were collected in 1996 and 2001 respectively. In contrast, drifters data are rather well distributed seasonally with more than 14 000 observations during winter and

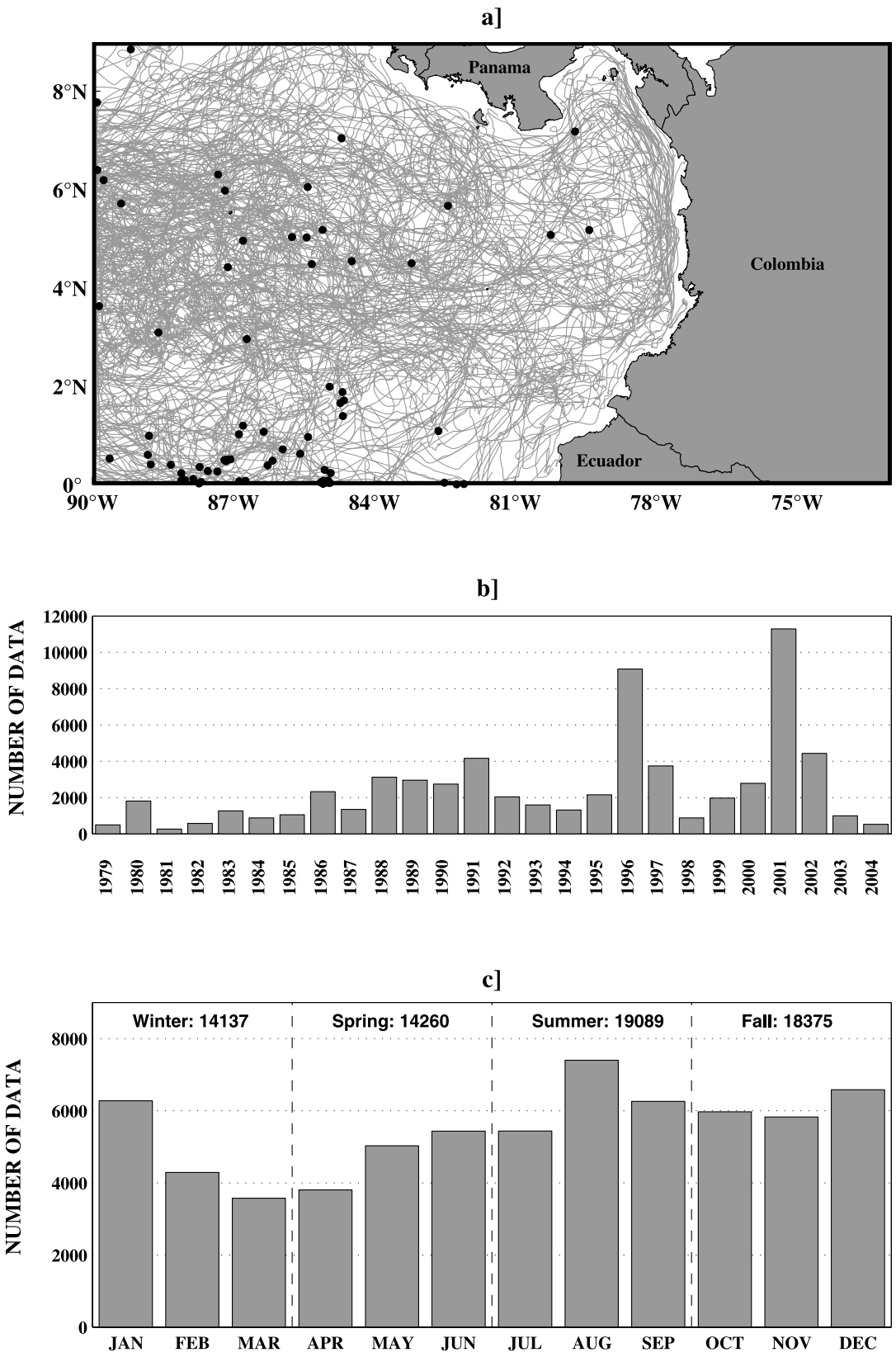

Figure 1. Spatio-temporal distribution of the near-surface drifter data used in this study. (a) Spaghetti diagram of the 250 drifter trajectories crossing the region during 1979–2004. Black dots correspond to initial positions of the 72 drifters deployed inside the region. (b) Number of 6h buoy data per year from 1979 to 2004. (c) Number of 6h buoy data per month for the 12 months of the year based on the 25 years of data. Solid black numbers indicate the seasonal repartition of the 6h buoy data.

spring months and around 18 000–19 000 for summer and fall (Figure 1c). This Lagrangian drifters data set is thus well suited to analyze the mean surface circulation and its seasonal variability.

2.3. Averaging Scales

[11] Ocean currents are commonly decomposed as the sum of a mean current $\overline{U}$ and a turbulent fluctuation velocity $\boldsymbol{u}'$ linked with temporal and small-scale variabilities. An important problem for analyzing surface current and turbulence properties is the choice of the spatial scale used to derive $\overline{U}$. Effectively, if the space-scales of averaging are not well estimated then the shears of the mean current are badly resolved and both the residual velocity field $\boldsymbol{u}'$ and the Lagrangian statistics are affected (see section 5). These space-scales of averaging are a compromise between high resolution of the current shears and high number of data per bin, in order to obtain accurate estimates of the mean currents.

[12] The lower limit should be chosen such that two consecutive observations may not be separated by more than a bin [*Poulain*, 2001]. Considering a maximum velocity of 1.5 m s^{-1}, the maximum displacement between two consecutive observations separated by 6 h is of the order of 30–35 km. Figure 2a shows the dependence of the mean and eddy kinetic energies (MKE and EKE respectively) on the bin averaging scale. MKE and EKE are computed considering only ''significant'' bins passing the following tests: (1) each of the four seasons is represented; (2) less than 25% of the bin area corresponds to land; (3) the number of independent observations N^* (see below for definition) is greater than or equal to 3.

[13] Note that while these three criteria are also necessary to represent adequately the surface circulation, only criteria 2 and 3 are required for the seasonal circulation and during ENSO periods. Both the MKE and EKE decrease for resolution higher than 0.1° due to the small number of data considered (Figure 2a), as also observed in the Adriatic Sea by *Maurizi et al.* [2004]. Maxima of about 250 cm^2 s^{-2} and 600 cm^2 s^{-2} respectively are reached for a resolution of 0.1°–0.2°. For lower resolutions, MKE and EKE decrease asymptotically to near constant values of 130 cm^2 s^{-2} and 570 cm^2 s^{-2} respectively. Thus, the distribution of energies as a function of resolution suggests that the optimal resolution should be in the order of 0.2°. However, at this relatively high resolution only 45% of the bins successfully pass the three criteria (dashed line on Figure 2a) and only 65% of the data are considered (dashed dotted line on Figure 2a). For this reason and with a lower limit estimated to 30–35 km (~0.3°), we prefer to use a lower resolution, arbitrarily chosen such as at least 90% of available data and available bins were used. This choice corresponds to a bin size of 0.6° × 0.6° (Figure 2a) equivalent to ~65 km south of 9°N. At this resolution, the mean MKE and EKE values are ~170 cm^2 s^{-2} and ~570 cm^2 s^{-2} respectively. This corresponds to a drop of ~20% and ~3% relative to their values at the optimum resolution of 0.2° × 0.2°.

[14] Each observation separated by more than two times the Lagrangian temporal scale **T** can be considered uncorrelated and thus independent [*Flierl and McWilliams*, 1977]. Using all the available data and a maximum decorrelation scale of 8 days (**T** < 4 days, see section 5), the geographical distribution of the number of independent observations N^* were computed over a 0.6° × 0.6° resolution (Figure 2b). As was shown qualitatively in Figure 1a, a greater number of independent data is observed between 3°N–7°N and west of 81°W, but also in the southwest of the domain and along the Colombian coast. In contrast, fewer independent data are located off Ecuador, along the Panama coast and in the north-western corner of the region.

[15] The goal of this study is to give insight into the mean surface circulation and the mean Lagrangian properties, but also to examine their changes at seasonal timescale and during ENSO events. However, as noted before (section 2.2) the number of independent data is yearly dependent and the bin size must be adapted accordingly. A similar sensitivity dependence study (not shown) and the spatio-temporal data distribution suggest that an appropriate resolution for such temporal scales (seasonal and ENSO events) is 1° × 1°. Hereafter, the results presented at annual scale are thus based on 0.6° × 0.6° resolution bins, whereas results related to seasonal scales or ENSO events are based on 1° × 1° grid cells.

3. Near-Surface Flows

3.1. Mean Circulation

[16] The primary research issue is the determination of the mean surface currents of the Panama Bight and surrounding regions. As a first glance at the surface circulation, Figure 3a shows three selected trajectories entering the domain at approximately the same location between 5°N and 6°N and 90°W but showing different displacements. The first trajectory (dashed line on Figure 3a) flows eastward for ~5 days and is then progressively deflected northeastward along the western edge of the Cocos Ridge extending from the southwestern corner of the study region to the Panama coast at ~84°W. This buoy exits the domain close to the Costa Rica coast after 20 days of displacement. In contrast, the second trajectory (solid line on Figure 3a) is deflected northeastward along the eastern edge of the Cocos Ridge after 20 days of displacement and reaches the Coiba island region (between 81°W and 82°W) 40 days later. It is then deflected southward for ~12 days along a bathymetry ridge, before looping into the Panama Bight Cyclonic Gyre (PBCG) for two months and then ceasing to emit around the Pearl Archipelagos at ~8°N. Finally, the third trajectory (dotted line on Figure 3a) flows southeastward for nearly two months before being advected westward and exiting the study region at around 1°N–90°W.

[17] Figure 3b shows the mean surface circulation obtained from satellite-tracked drifters on the 0.6° × 0.6° grid cells following the three criteria mentioned in section 2.3. Almost 70% of the bins have more than 30 independent data and 90% more than 20 (pie chart in Figure 3b). The region is characterized by the presence of the relatively broad (~300 km) eastward North Equatorial Counter Current (NECC) entering the region north of 5°N. Upstream of the Cocos Ridge, a part of the NECC is deflected northward along the southern edge of the Costa Rica Dome to form the Costa Rica Coastal Current which flows into the large scale westward North Equatorial Current [*Tomczak and Godfrey*, 1994; *Fiedler*, 2002a]. Another part of the NECC crosses the Cocos Ridge between 5°N and 7°N, enters the Panama

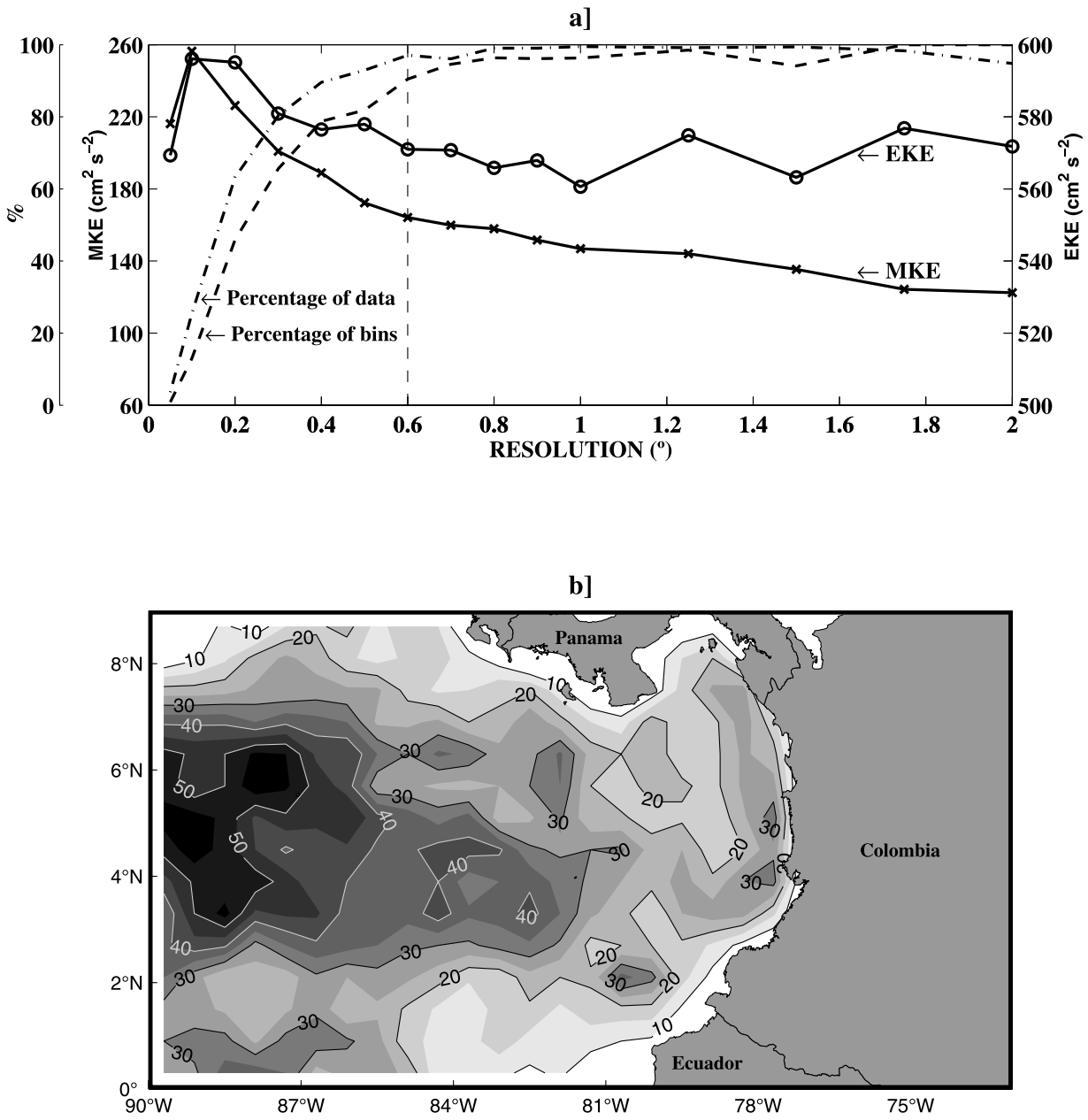

Figure 2. (a) Binned mean kinetic energy (MKE, crosses) and eddy kinetic energy (EKE, open circles), as a function of bin resolution. Also indicated are the percentage of considered bins (dashed line) and the percentage of data used in the estimates (dotted dashed line), as a ratio of data belonging to considered bins (see text) and the total number of data (65 656). Vertical dashed line corresponds to the spatial resolution of 0.6° × 0.6° chosen to compute the near-surface characteristics of the mean flow. (b) Spatial distribution of independent observations per 0.6° × 0.6° bins.

Basin and is then deflected southward at ∼81°W along a ridge to feed the PBCG. This cyclonic gyre was previously observed, in particular from hydrographic data [*Wooster*, 1959; *Stevenson*, 1970], from ship-drifts [*Fiedler*, 2002a], and from satellite measurements [*Rodríguez-Rubio et al.*, 2003]. Here we show that the PBCG also has a clear signature on the surface currents observed from satellite tracked drifters and that it is strongly confined to the bathymetric features shallower than 2500 m depth. Finally, another part of the NECC is deflected southeastward at around 85°W and between 4°N–6°N and turns westward south of 2°N–3°N between the coast and 84°W to feed the South Equatorial Current (SEC).

[18] Averaging more than 65 000 velocity magnitudes, the surface current in the whole study region has a mean speed exceeding 30 cm s^{-1} (Table 1). However, averaging both velocity components, the mean velocity vector has a magnitude of 6.5 cm s^{-1} and is oriented 12° south of east.

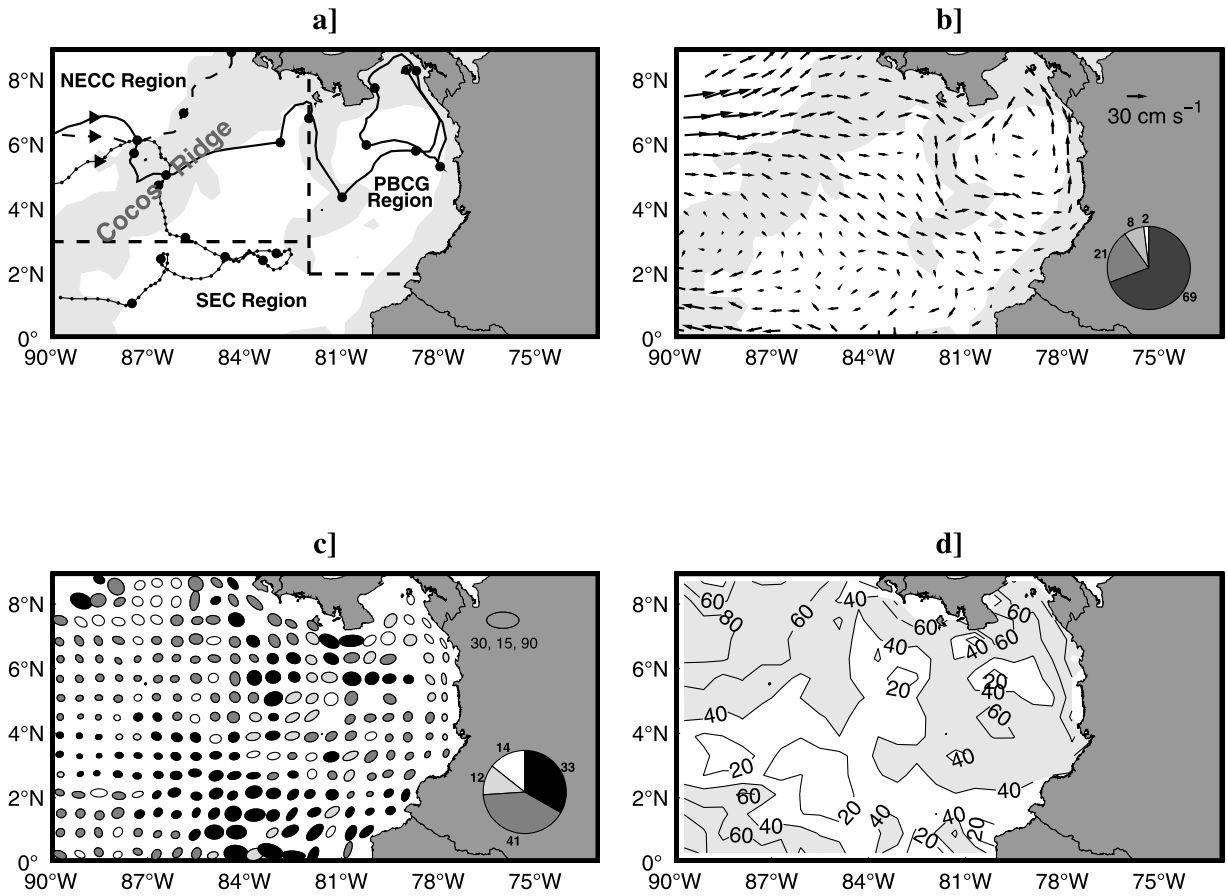

Figure 3. Mean characteristics of the near-surface circulation. (a) Examples of surface buoy trajectories highlighting the principal features of the mean currents; each 10 day position is indicated by a full circle. Range of 0–2500 m depth is shaded grey. Northern Equatorial Counter Current (NECC), Panama Bight Cyclonic Gyre (PBCG) and South Equatorial Current (SEC) regions are delimited by dashed black lines. (b) Mean surface circulation obtained from satellite-tracked drifters in considered bins of $0.6^\circ \times 0.6^\circ$. Arrows are centered at the center of mass of the observations in each bin and range of 0–2500 m depth is shaded grey. From white to black, pie parts indicate the percentage of bins having less than 3, 3 to 10, 10 to 20 and more than 20 independent observations, respectively. (c) Velocity error ellipses (see Appendix A), also centered at the center of mass of the observations in each considered bin of $0.6^\circ \times 0.6^\circ$. The scale ellipse has a semimajor axis of 30 cm s^{-1}, a semiminor axis of 15 cm s^{-1} and is rotated 90° from north. Open ellipses indicate that errors are lower than the mean velocity for both velocity components ($\varepsilon_u < U$ and $\varepsilon_v < V$). Light (dark, respectively) grey shaded ellipses indicate that $\varepsilon_u > U$ and $\varepsilon_v < V$ ($\varepsilon_u < U$ and $\varepsilon_v > V$), while black shaded ellipses indicate that errors are higher than the velocity for both components ($\varepsilon_u > U$ and $\varepsilon_v > V$). (d) Directional stability (in %). Regions with stability values higher than 40% are shaded.

Based on the three different buoy behaviors depicted on Figure 3a and on the mean surface circulation shown on Figure 3b, the study region can be divided into three subregions (Figure 3a) characterized by distinct circulation features: (1) The NECC Region, north of 3°N and west of 82°W, which encompasses the predominantly eastward NECC; (2) The PBCG Region, east of 82°W and north of 3°N, characterized by cyclonic circulation; and (3) the SEC Region, including the westward South Equatorial Current (Table 1). The PBCG has an apparent diameter of ~400 km and a typical radial velocity magnitude of ~30 cm s^{-1}. This corresponds to a rotation period of approximately 50 days, which roughly coincides to the time spent in the Panama Bight by the second trajectory shown on Figure 3a (solid line). Rotary spectrum obtained from time-series of drifter velocity components shows a slightly higher level of energy in the clockwise rotation sense for frequency of ~0.5 cycle per month (not shown), most probably influenced by the PBCG. The clockwise component is also 2 to 10 times more energetic than the anticlockwise component over the broad range of frequencies of 4–12 cycles per months, corresponding to inertial motions.

[19] It should be borne in mind that when dealing with satellite-tracked drifters, the obtained near-surface circula-

Table 1. Statistics for the Whole Study Region, the North Equatorial Counter Current (NECC), the Panama Bight Cyclonic Gyre (PBCG), and the South Equatorial Current (SEC)[a]

	N*	$\lvert\overline{U}\rvert \pm \Delta\lvert\overline{U}\rvert$, cm s^{-1}	$U \pm \Delta U$, cm s^{-1}	$V \pm \Delta V$, cm s^{-1}	Angle, °T	σ_u, cm s^{-1}	σ_v, cm s^{-1}	$\overline{u'v'}$, cm^2 s^{-2}
				Global Region [0–9°N; 73°W–90°W]				
Annual	2236	31.2 ± 0.8	6.3 ± 1.2	−1.3 ± 1.0	101.7 (SE)	28.4	22.6	14.8
Normal	2002	29.8 ± 0.8	6.7 ± 1.2	−2.3 ± 1.0	108.9 (SE)	26.9	21.8	14.4
Niño	506	31.3 ± 1.7	5.0 ± 2.5	−0.1 ± 2.0	91.1 (SE)	28.5	22.7	8.6
Niña	741	32.9 ± 1.5	6.5 ± 2.2	−0.7 ± 1.7	96.1 (SE)	30.1	23.4	20.9
				NECC Region [3–9°N; 82°W–90°W]				
Annual	1270	32.9 ± 1.1	12.9 ± 1.6	−1.9 ± 1.3	98.4 (SE)	28.2	22.9	14.0
Normal	596	31.8 ± 1.6	13.5 ± 2.2	−3.0 ± 1.8	102.5 (SE)	26.6	22.5	20.7
Niño	276	33.1 ± 2.2	10.5 ± 3.3	0.2 ± 2.8	88.9 (NE)	27.7	23.7	−9.9
Niña	509	34.4 ± 1.9	13.6 ± 2.7	−1.7 ± 2.0	97.1 (SE)	30.7	22.7	24.6
				PBCG Region [2–9°N; 73°W–82°W]				
Annual	495	29.7 ± 1.6	5.5 ± 2.2	0.4 ± 2.2	85.8 (NE)	24.7	24.2	−0.1
Normal	180	29.1 ± 2.6	7.3 ± 3.5	−0.3 ± 3.6	92.4 (SE)	23.2	23.9	−26.2
Niño	132	27.2 ± 2.9	3.9 ± 3.9	1.8 ± 3.8	65.2 (NE)	22.7	22.1	5.1
Niña	185	32.2 ± 2.9	4.9 ± 4.0	0.0 ± 3.8	90.0 (E)	27.3	25.7	24.4
				SEC Region [0–3°N Between 82°W–90°W and 0–2°N Between 73°W–82°W]]				
Annual	673	28.7 ± 1.4	−7.0 ± 2.1	−1.4 ± 1.6	258.7 (SW)	26.7	20.3	36.0
Normal	316	26.2 ± 1.9	−7.2 ± 2.7	−2.3 ± 2.1	252.3 (SW)	24.4	18.7	35.1
Niño	142	31.9 ± 3.7	−5.9 ± 5.5	−3.0 ± 3.5	243.0 (SW)	32.5	20.6	21.5
Niña	217	30.4 ± 2.3	−7.5 ± 3.5	0.9 ± 3.0	276.8 (NW)	26.0	22.3	49.1

[a]These were obtained from drifter data sets for the whole 1979–2004 period (annual), for the ENSO periods and for normal conditions without ENSO events (see text for details). *N** represents the number of independent observations. Angles of the mean flows are given in terrestrial degrees relative to the north.

tion is a combination of geostrophic flow and of ageostrophic currents associated with Ekman drift [*Niiler and Paduan*, 1995; *Ralph and Niiler*, 1999; *Niiler*, 2001]. However, due to the proximity of the equator, where Ekman theory and geostrophic balance break down, these two components were not computed separately. Nevertheless, with surface currents typically in the order of 30 cm s^{-1} (Table 1) and reaching speeds as fast as 1.5 m s^{-1}, we expect that the near-surface mean flow in the study region is mainly geostrophic. Furthermore, the circulation derived from drifter data is also contaminated by other factors such as the wind-induced slip of the drogue [*Niiler et al.*, 1987], positioning errors or the "array bias" [*Davis*, 1991]. The circulation was not corrected for these different potential errors, as discussed in Appendix A. Principal axes of velocity error ellipses, due to sampling error, were computed in each grid-cell (Figure 3c) from the eigenvalues and eigenvectors of the velocity covariance matrix (see Appendix A) [*Emery and Thomson*, 1998]. The method is similar to that of the computation of variance ellipses [*Morrow et al.*, 1994; *Le Traon and Morrow*, 2001]. In the study region, error ellipses suggest that the flow is slightly anisotropic with a zonal elongation observed principally south of 4°S and an alongshore elongation of the coastal currents. This anisotropy is quantitatively confirmed in Table 1: except in the PBCG region, all regions exhibit variances 20–25% greater in the zonal than in the meridional direction. For the whole study region the mean velocity errors ± one standard deviation are 10.0 ± 3.2 cm s^{-1} and 8.6 ± 2.4 cm s^{-1} for the zonal and meridional directions respectively. However, around 15% of the bins (Figure 3c) show velocity errors lower than the mean flow along each component ($\varepsilon_u < U$ and $\varepsilon_v < V$). In contrast, 50% of the bins show important velocity errors in a specific direction ($\varepsilon_u > U$ or $\varepsilon_v > V$): regions where $\varepsilon_u > U$ (light shading on Figure 3c) correspond principally to the eastern and western sides of the PBCG where zonal currents are weak, while regions where $\varepsilon_v > V$ (dark shading on Figure 3c) are principally associated with quasi zonal currents (NECC, SEC and southern flank of PBCG) showing a weak meridional component. Finally 33% of the bins, showing $\varepsilon_u > U$ and $\varepsilon_v > V$ (black shading on Figure 3c), correspond to regions of relatively weak current (Figure 3b) or with a small number of independent data (Figure 2b).

[20] Figure 3d shows the directional stability of the mean flows corresponding to the ratio of the magnitude of the mean velocity vector and the average speed [*Brugge*, 1995; *Carr and Rossby*, 2001]. A persistent direction of the flow corresponds to high stability values, whereas a zero value corresponds to random motion. The average stability of the study region is almost 50% and the main circulation features are persistent during the 1979–2004 time period with directional stability values higher than 40% for the NECC, the PBCG and the SEC. Values higher than 60–80% are observed in the northwest and southwest of the study region and along the coasts of North Columbia and Panama where the strongest currents are observed. In contrast, values lower than 20% are observed in regions of weak currents such as the centre of the PBCG and the transition zone between NECC and SEC.

3.2. Temporal Variations

[21] As noted in section 1, the upper circulation of the tropical Pacific Ocean is strongly influenced by seasonal variations and by ENSO events [*Reverdin et al.*, 1994; *Johnson et al.*, 2000, 2002]. The goals of this section are thus to investigate to what extent the mean surface circulation presented above varies at seasonal scales, as well as to

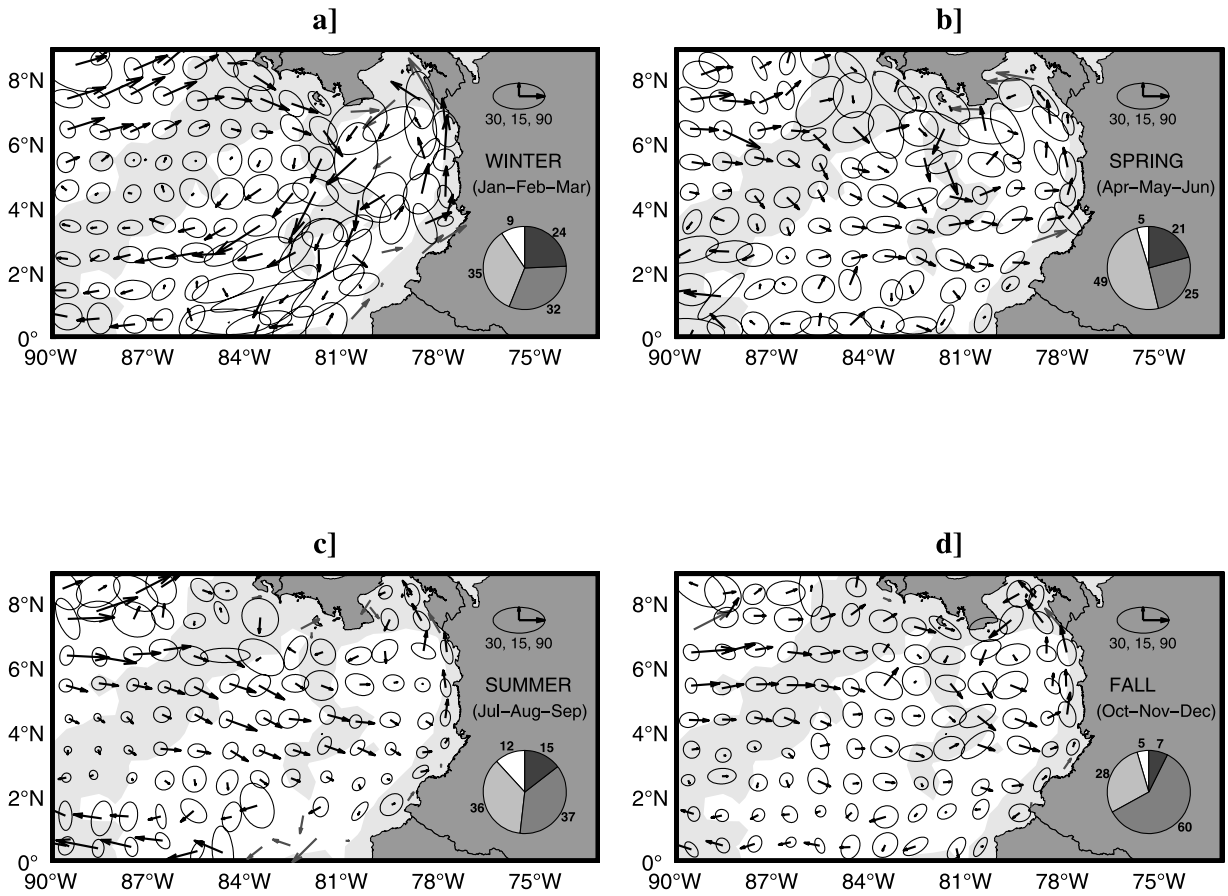

Figure 4. Seasonal maps of mean surface circulation and velocity error ellipses. Arrows and ellipses are centered at the center of mass of the observations in each considered bin of 1° × 1° and the 0–2500 m depth range is shaded grey. Scale ellipses have a semimajor axis of 30 cm s^{-1}, a semiminor axis of 15 cm s^{-1} and are rotated 90° from north. From white to black, pie parts indicate the percentage of bins having less than 3, 3 to 10, 10 to 20 and more than 20 independent observations, respectively.

determine how the mean upper circulation observed from satellite-tracked drifters is affected or biased by ENSO events.

3.2.1. Seasonal Variability

[22] West of 90–100°W, the variability of oceanic properties has been extensively studied based on hydrographic and mooring measurements [*Gu et al.*, 1997; *Yu and McPhaden*, 1999; *Cronin and Kessler*, 2002; *Kessler*, 2006], satellite data [*Palacios*, 2004], or satellite tracked drifters [*Reverdin et al.*, 1994]. In contrast, in the study region east of 90°W, few studies have recently given insight into this topic. For example, *Fiedler* [2002a] has depicted the monthly surface circulation in the Panama Bight and Costa Rica Dome regions based on ship drifts; *Rodríguez-Rubio et al.* [2003] have described the seasonal variability of the PBCG geostrophic circulation based on altimetry measurements; and *Kessler* [2006] gives a review of the ESP circulation based on different measurements without focusing especially on the Panama Bight surrounding regions. Here we thus provide an independent picture of the seasonal variability of the near-surface circulation, based on satellite tracked drifters data.

[23] In winter (January to March), the region is characterized by the presence of an anticyclonic gyre in the west and a cyclonic gyre in the east (Figure 4a). The southern edge of the PBCG is however not well marked and is found around 2–3°N. The anticyclonic cell, bounded by the NECC to the north and by the SEC to the south, is centered at ~85°W–5°N. At around 81°W, this cell joins the PBCG to form an intense southwestward jet where speeds higher than 50 cm s^{-1} are commonly observed. This strong ~200 km wide southward current, also observed from altimetry measurements [*Rodríguez-Rubio et al.*, 2003], is associated with high velocity variances suggesting high levels of eddy kinetic energy. In the three subregions, the surface currents are of the order of 40 cm s^{-1}, ~20% stronger than the annual mean (Table 2). The near-surface circulation observed during winter is mainly controlled by the atmospheric Panama jet and the associated wind-stress curl. In spring (April to June), the Panama jet is greatly reduced and as a result, the anticyclonic cell is no longer maintained and the NECC flows southeastward from 90°W–7°N to 80°W–3°N until the southern flank of the PBCG (Figure 4b). During this season, the surface circulation in the Panama Bight shows a well marked cyclonic

Table 2. Seasonal Statistics (as in Table 1) for the Whole Basin, the NECC, the PBCG, and the SEC Regions

	N*	$\lvert\overline{U}\rvert \pm \Delta\lvert\overline{U}\rvert$, cm s^{-1}	$U \pm \Delta U$, cm s^{-1}	$V \pm \Delta V$, cm s^{-1}	Angle, °T	σ_u, cm s^{-1}	σ_v, cm s^{-1}	$\overline{u'v'}$, cm^2 s^{-2}
				Global Region [0–9°N; 73°W–90°W]				
Winter	507	38.6 ± 2.0	0.8 ± 3.2	0.0 ± 2.5	90.0 (E)	35.6	27.8	126.5
Spring	692	34.7 ± 2.6	11.5 ± 2.2	−2.6 ± 1.8	102.7 (SE)	29.1	23.9	11.1
Summer	667	25.9 ± 1.2	7.1 ± 1.8	−2.6 ± 1.4	120.1 (SE)	23.0	18.6	−32.9
Fall	645	28.2 ± 1.4	5.6 ± 2.0	0.1 ± 1.6	89.0 (NE)	25.6	20.5	−6.0
				NECC Region [3–9°N; 82°W–90°W]				
Winter	355	38.3 ± 2.4	7.3 ± 3.7	1.7 ± 2.9	76.9 (NE)	34.8	27.5	90.0
Spring	289	36.9 ± 2.2	15.4 ± 3.5	−5.3 ± 2.9	109.0 (SE)	29.5	24.6	13.2
Summer	366	27.1 ± 1.7	14.7 ± 2.2	−5.0 ± 1.8	118.8 (SE)	21.5	17.6	−1.0
Fall	304	30.0 ± 2.0	14.8 ± 2.8	0.9 ± 2.3	86.5 (NE)	24.7	19.9	−22.2
				PBCG Region [2–9°N; 73°W–82°W]				
Winter	58	41.3 ± 5.8	−3.6 ± 7.9	−6.9 ± 9.3	207.6 (SW)	30.1	35.3	86.8
Spring	106	32.3 ± 3.2	12.5 ± 4.8	2.4 ± 4.5	79.1 (NE)	24.7	23.4	−46.2
Summer	201	24.0 ± 2.0	4.9 ± 2.7	0.6 ± 2.8	83.0 (NE)	19.1	19.8	−22.0
Fall	155	32.0 ± 3.2	4.8 ± 4.5	1.3 ± 4.0	74.8 (NE)	28.1	25.1	0.5
				SEC Region [0–3°N Between 82°W–90°W and 0–2°N Between 73°W–82°W]]				
Winter	146	38.1 ± 3.9	−16.2 ± 5.6	−1.9 ± 4.1	263.3 (SW)	34.1	24.6	172.1
Spring	168	32.1 ± 2.8	3.3 ± 4.6	−0.6 ± 3.4	100.3 (SE)	29.6	22.1	80.0
Summer	152	25.7 ± 2.7	−11.1 ± 3.6	−1.2 ± 3.0	263.8 (SW)	22.3	18.4	−54.6
Fall	226	23.1 ± 1.8	−6.4 ± 2.5	−1.9 ± 2.3	253.5 (SW)	19.1	17.4	−21.3

gyre where the southern edge is centered at ∼4°N. In the PBCG and SEC regions the average surface speeds are reduced by 5–10 cm s^{-1} to their winter values, whereas in the NECC region they are unchanged (Table 2). Maximum velocity error ellipses are now located along the Panama coasts and in the SEC region where the current does not show a well-defined direction. In summer (July to September), surface currents are greatly weakened and typical values of 25 cm s^{-1} are observed in the three sub-regions. The NECC separates into two branches (Figure 4c): the first one north of 8°N flows northeastward to feed the Costa Rica Coastal Current, whereas the second branch shows a clear southeastward direction flowing almost to the Colombian coast at 3–4°N. The SEC during this season has a well-defined westward orientation. During summer months, maximum velocity error ellipses are found in the northwest and southwest parts of the domain. Finally in fall (October to December), the NECC flows eastward centered at ∼6°N. At around 84°W, a part of this current is slightly deflected northeastward and feeds the western branch of the PBCG, while another part of the NECC flows southeastward feeding the southern edge of the PBCG at ∼4°N. During this season, velocity errors are relatively weak in the whole domain and surface currents in the NECC and PBCG regions increase to 30 cm s^{-1}, whereas they reach their minimum values in the SEC region (Table 2). Figure 4 and Table 1 suggest a semiannual cycle for the SEC, with maximum westward currents in winter and summer and minimum during spring and fall. This result extends the ones of *Reverdin et al.* [1994] who also observed significant semiannual energy in the SEC further west in the central Pacific.

3.2.2. Influence of El Niño/La Niña Events

[24] The impact of ENSO events on the near-surface circulation is investigated using only surface drifter velocities corresponding to El Niño, La Niña, or ''normal'' periods (in this case not including the data corresponding to ENSO events). The phases of the warm (El Niño) or cold (La Niña) ENSO periods are identified by adapting the criteria given by *Trenberth* [1997] initially for the Niño3.4 region (5°S–5°N and 170°W–120°W) to the Niño3 region (5°S–5°N and 150°W–90°W) located west of the study region. An El Niño (La Niña, respectively) event is identified if the 5-month running-average of the Niño3 Index exceeds 0.4°C (−0.4°C) for at least 6 consecutive months. Figure 5a shows the monthly distribution of the number of drifter data from 1979 to 2004 and the temporal evolution of this Niño3 Index computed from the monthly NCEP/NCAR sea surface temperature time series (http://www.cpc.ncep.noaa.gov/data/indices/). Warm (cold, respectively) ENSO events associated with El Niño (La Niña) are shaded black (light grey), whereas regular periods are depicted by dark grey shading. Since the 1980s, strong El Niños occurred in 1982–83, 1986–87, 1997–98 (82–83 and 97–98 being catalogued as very strong or exceptional) and weak events in 1991–92 and 2002–03. La Niñas occurred in 1984–85, 1988–89 and 1998–2000, with a weaker event in 1995–96. Of the 65 000 drifter data (Figure 5a, bottom), 22% (∼15 000 data) are observed during relatively warm El Niño periods, 33% (∼20 000 data) during relatively cold La Niña periods and 45% (∼30 000 data) in ''normal'' or ''regular'' conditions. These different conditions are very well sampled, since a uniformly distributed data set over 1979–2004 would show 24%, 29% and 47% during these respective periods, as also observed by *Trenberth* [1997] in the Nino3.4 region. Similarly, ENSO periods are not strongly biased toward a specific season of the year since each season is sampled by 18%–33% of the data during El Niño periods and by 22%–28% during La Niña periods.

[25] Figures 5b–5d show the mean near-surface circulations obtained on 1° × 1° grid cells for normal conditions and during the relatively warm and cold ENSO periods. During El Niño periods, around 45% of the bins contain between 3 and 10 independent data, whereas during normal

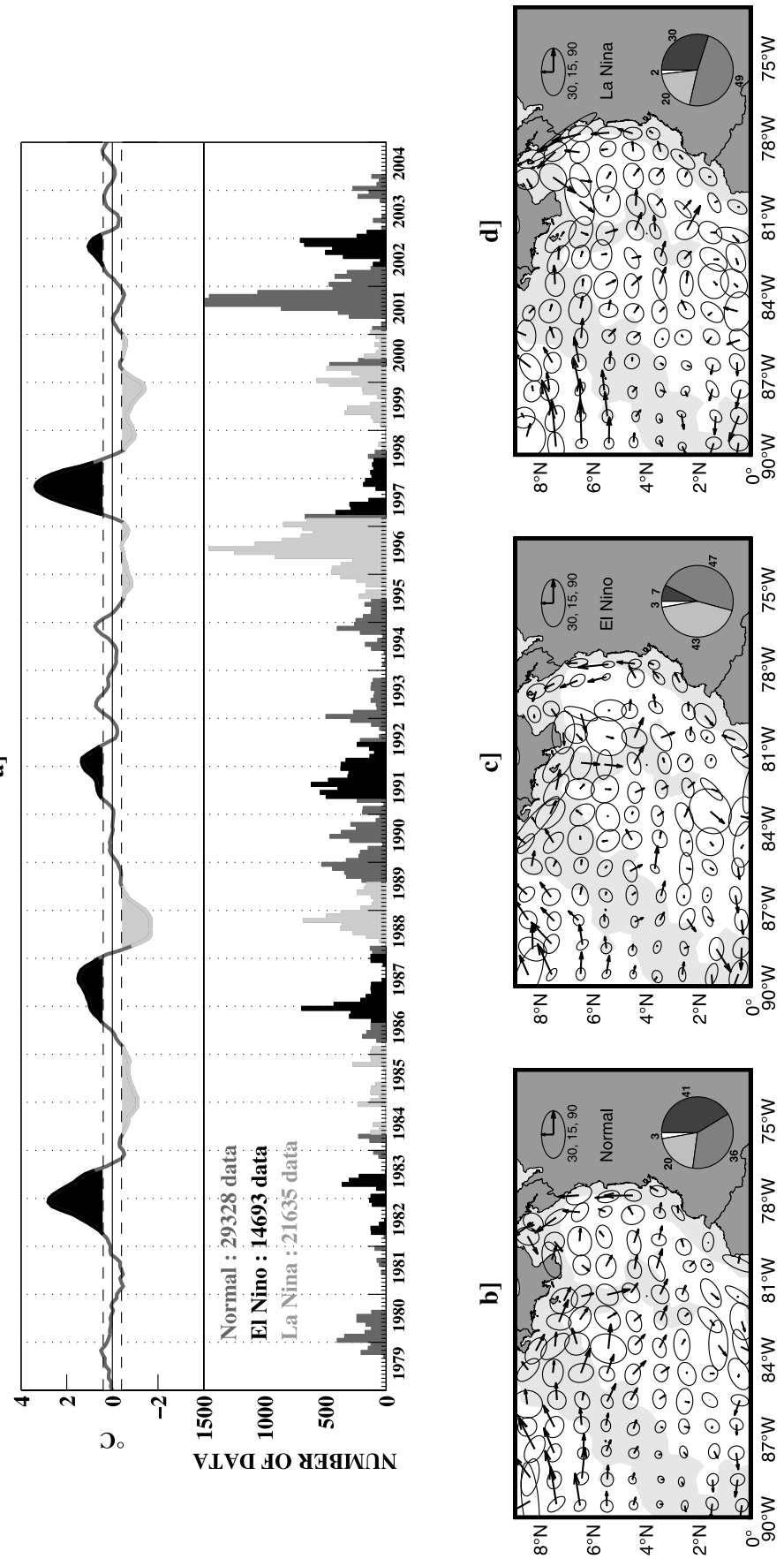

Figure 5. Distribution of the drifter data and mean circulation at interannual scales. (a) Niño3 Index computed from the monthly NCEP/NCAR sea surface temperature time series (see text) and monthly distribution of 6h drifter data between 1979 and 2004. Black (light grey, respectively) shade corresponds to El Niño (La Niña) periods whereas dark grey shade corresponds to "normal" conditions. (b)–(d) Surface circulation and velocity error ellipses computed from drifter data during "normal", El Niño and La Niña periods. Arrows and ellipses are centered at the center of mass of the observations in each bin and the 0–2500 m depth range is shaded grey. Scale ellipses have a semimajor axis of 30 cm s^{-1}, a semiminor axis of 15 cm s^{-1} and are rotated 90° from north. From white to black, pie parts indicate the percentage of bins having less than 3, 3 to 10, 10 to 20 and more than 20 independent observations, respectively.

and La Niña conditions, around 80% of the bins contain more than 10 independent data. In the central and western tropical Pacific, the SEC during El Niño events is greatly weakened, whereas the NECC is strengthened [*Philander*, 1990; *Johnson et al.*, 2000, 2002]. In the NECC region between 81°W–86°W, the eastward/south-eastward surface circulation is much less marked during El Niño events (Figure 5c) than during normal and La Niña periods (Figures 5a–5d). Table 1 indicates that the eastward component of the NECC is weakened by ~3 cm s^{-1} during El Niño and is oriented slightly northeastward (~89°T) during these warm periods. No significant differences are observed in the NECC region between normal and La Niña conditions. In contrast to what is observed in the main part of the equatorial Pacific, but agreeing with what was observed during the 1990s at 95°W by *Johnson et al.* [2000, 2002] and *Grodsky and Carton* [2001], the westward SEC east of 90°W is reinforced by 15–20% during both the El Niño and La Niña events (Figure 5 and Table 1). The PBCG is only slightly weakened (strengthened, respectively) during El Niño (La Niña) periods (see also Table 1). Thus, around the Panama Bight east of 90°W, ENSO conditions do not strongly modify the mean surface circulation observed during normal periods (Figure 5), as also suggested by a James' test at the 5% significance level, which indicates that only ~1/3 of the bins show significant differences between ENSO and normal periods, principally in the NECC region. Finally, in each sub-region, both the velocity components present a standard deviation in the range of 20–30 cm s^{-1}, corresponding to eddy kinetic energy in the order of 400–600 cm^2 s^{-2}. During cold La Niña periods, these deviations are slightly higher whereas during warm El Niño periods they are mainly unchanged, except in the SEC Region, where zonal elongation is enhanced.

4. Kinematics: Energies and Surface Vorticity

[26] Since the apparition of satellite observations, it has become apparent that mesoscale processes, responsible for turbulent diffusion and the redistribution of heat, salt and suspended materials [*Bryden and Brady*, 1989; *Jayne and Marotzke*, 2002] can have a very significant impact on larger scales [*Van Haren et al.*, 2004]. Based on the previously depicted surface circulation and its variability, mean kinetic and eddy kinetic energies are shown in Figure 6. Kinetic energy associated with the mean surface currents has values lower than 100–200 cm^2 s^{-2} over the study region (Figure 6a), except in the northwest and southwest parts of the domain where mean currents are stronger (Figure 3b). Values of MKE higher than 300 cm^2 s^{-2} are also observed around the PBCG where surface currents are of the order of 30 cm s^{-1}. In contrast, EKE associated with temporal variations of the surface currents shows a mean value of order of 600 cm^2 s^{-2} in the study region (Figure 6b). Maxima of EKE are observed in the central region where the NECC penetrates seasonally in the Panama Bight and where the Panama wind jet is known to extend [*Chelton et al.*, 2000a; *Chelton*, 2000]. The cluster of high values found at 1°N and 84°W is due to important velocity variance particularly observed during winter (Figure 4b). This EKE intensity is around two times higher than the geostrophic EKE computed from satellite altimetry measurements (not shown) as is also observed in different regions of the world-ocean [*Ducet et al.*, 2000; *Martins et al.*, 2002; *Chaigneau and Pizarro*, 2005]. The cluster of high positive values observed in the central region (Figure 6b) is also located slightly further east on altimetry maps. Differences between the two data sets are probably due to the fact that satellite data refers to the geostrophic component of the flow only, whereas the drifter EKE also includes the ageostrophic component and higher frequencies associated with inertial and tidal motions.

[27] Total kinetic energy (MKE + EKE) associated with the surface circulation is thus largely dominated by the EKE except along the north Colombian coast where the northward branch of the PBCG is found and in the northwest and southwest parts of the study region (Figure 6c). The percentage of the total energy explained by the EKE (Figure 6c) is strongly anti-correlated with the distribution of directional stability (Figure 3d): the stronger the directional stability, the lower the temporal variability of the current and hence the associated EKE. On average over the region, EKE represents 80.5% of the total energy and values higher than 90% are principally observed in regions of weak mean current (Figure 3b) and weak directional stability (Figure 3d), corresponding to the center of the PBCG and to a band extending from the Ecuadorian coasts to 4°N and 90°W. The Panama Bight and surrounding regions are thus an important area of eddy activity generated by different processes such as the instability of the mean currents, the interaction of the current system with the topography, or most probably with the Panama wind jet increasing the turbulence in the upper oceanic layer [*Kessler*, 2006].

[28] In agreement with the mean surface circulation, levels of MKE are largely unchanged during ENSO periods (not shown). In contrast, the mean EKE in the study region increases slightly from ~500 cm^2 s^{-2} during normal periods to 570 cm^2 s^{-2} during both El Niño and La Niña events as was also suggested by the velocity variances (Table 1). EKE also shows more spatial variability than MKE during these different periods (not shown): during "normal" conditions, the spatial distribution of EKE is close to what is observed in Figure 6b; during El Niño events, strong levels of EKE are observed south of 3°N and west of 81°W, whereas lower levels are observed along the coasts; finally, during La Niña periods strong levels of EKE (>800 cm^2 s^{-2}) are observed in the northwestern part of the domain. More drifter data or numerical simulations from a high resolution regional model are needed to accurately interpret these slight interannual changes.

[29] At seasonal scales, total kinetic energy varies from a maximum of around 1200 cm^2 s^{-2} in winter to around 600 cm^2 s^{-2} during summer and fall (Figure 6d). Since both the MKE and EKE seasonal evolution show similar patterns in the three sub-regions, the NECC, PBCG and SEC regions are not discussed separately. Levels of EKE are always largely higher than MKE (Figure 6d), except during summer where both EKE and MKE contribute almost equally to the total energy. EKE is highest during winter (800 cm^2 s^{-2}) and lowest during summer (350 cm^2 s^{-2}), whereas MKE varies in a smaller range of 200–350 cm^2 s^{-2} and shows a semiannual cycle with local maxima during winter and summer and local minima during spring and fall. The EKE seasonal variability is closely related to the temporal

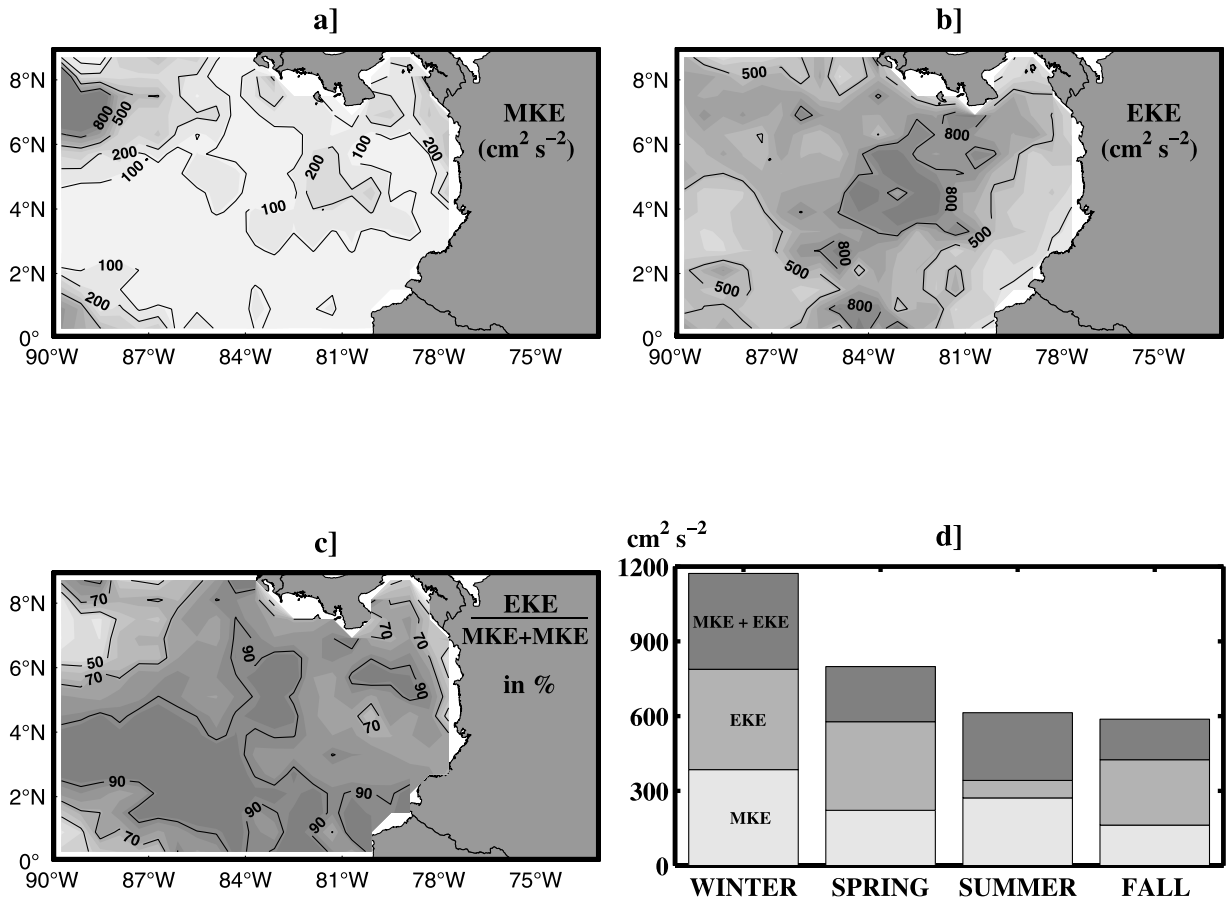

Figure 6. Spatial and seasonal distributions of near-surface kinetic energies. (a) Mean Kinetik Energy (MKE). (b) Eddy Kinetik Energy (EKE). (c) Percentage of total energy (MKE + EKE) accounted for the EKE. (d) Seasonal variations of MKE (blue), EKE (yellow) and total energy (red). Energies are in $cm^2\ s^{-2}$.

variability of the wind regime in the study region [*Rodríguez-Rubio et al.*, 2003], which can be an important source of mesoscale activity. Being highly energetic, mesoscale processes are efficient for horizontal mixing and lateral transport of physical and biogeochemical seawater properties.

[30] The dynamics of the upper ocean is also important since its relative vorticity can be an indicator of the vertical movements and of the upwelling of nutrient rich deeper water playing a substantial role in the biogeochemical properties and the trophic chain of the ocean [*McGillicuddy et al.*, 1998]. Relative vorticity ζ corresponds to the vertical component of the horizontal large-scale velocity curl:

$$\zeta = \frac{\partial V}{\partial x} - \frac{\partial U}{\partial y}$$

where $\mathbf{U} = (U, V)$ is the mean velocity and ∂x and ∂y are the eastward and northward distances. In the Northern Hemisphere, $\zeta > 0$ ($\zeta < 0$, respectively) is related to cyclonic (anticyclonic) circulation which is in part forced by positive (negative) wind-stress curl. Thus, a cyclonic (anticyclonic) circulation cell can be mainly associated with an upwelling (downwelling) of isopycnal levels and positive (negative) pumping.

[31] In the study region, an important pole of positive curl is logically observed in the PBCG with values higher than $4\ 10^{-6}\ s^{-1}$ locally (Figure 7a) corresponding approximately to one cycle per month. Two other patches of high vorticity are found in the southwest and in the northwest of the domain: the shear between the weak northeastward coastal current along Ecuador and the southeastward offshore current leads to positive vorticity values of the order of $1–2\ 10^{-6}\ s^{-1}$, whereas the cyclonic inflexion of the NECC toward the Costa Rica Coastal Current produces values higher than $2\ 10^{-6}\ s^{-1}$ in the southern edge of the Costa Rica Dome. In contrast small patches of negative vorticity are principally observed where the mean current shows weak anticyclonic cells southwest of Coiba Island (~7°N–83°W) and around 2°N and 84°W. The dipole formed by positive PBCG vorticities and negative patch centered at 7°N–83°W may also be related to the opposite sign of the wind stress curl on both flanks of the Panama jet. The vorticity does not change significantly between normal conditions and ENSO events (not shown), but depending on

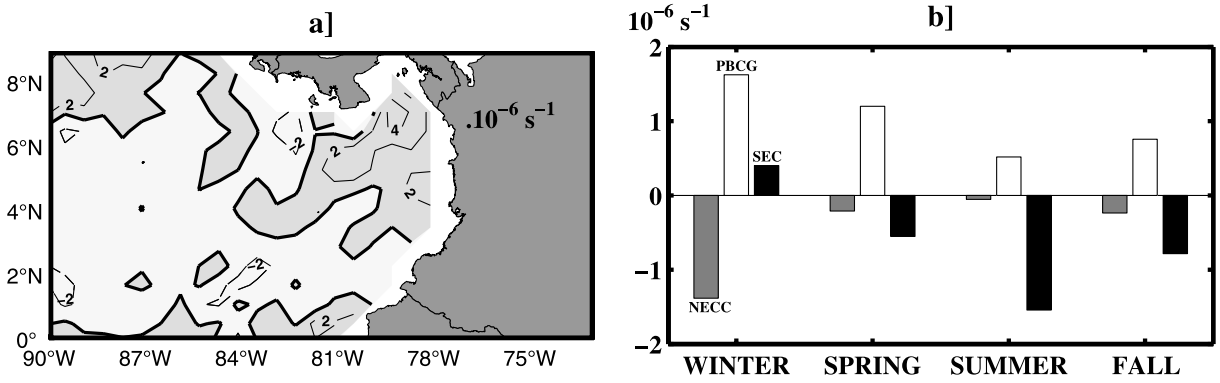

Figure 7. Spatial and seasonal distributions of near-surface vorticity. (a) Mean vorticity (in 10^{-6} s^{-1}) computed from near-surface drifters. Light (dark, respectively) shading corresponds to negative (positive) vorticity values. (b) Seasonal variation of the vorticity for the NECC, PBCG and SEC regions.

the considered sub-region, the vorticity shows distinct seasonal variability (Figure 7b) controlled in part by wind-stress curl variations. In the PBCG region the vorticity varies from a maximum positive value of around 1.7 10^{-6} s^{-1} in winter, which is also associated with a maximum positive wind stress curl at this season [*Chelton et al.*, 2000a; *Chelton*, 2000; *Rodríguez-Rubio et al.*, 2003], to a minimum of 0.5 10^{-6} s^{-1} in summer. The latter is related to the weakening of the gyre during spring and summer (Figure 4 and Table 2) when the intensity of the Panama wind jet decreases; this was also observed earlier from altimetry measurements [*Rodríguez-Rubio et al.*, 2003]. Conversely, in the NECC region the vorticity is strongly negative in winter (~ -1.5 10^{-6} s^{-1}) due to the presence of the important anticyclonic cell (Figure 4a). During the rest of the year, this cell disappears (Figures 4b–4d) and the vorticity in this region becomes negligible. Finally, in the SEC region the vorticity passes from a slightly positive value (~ 0.4 10^{-6} s^{-1}) in winter to strong negative ones (~ -1.8 10^{-6} s^{-1}) in summer. This change is probably induced by the shear between the southern edge of the eastward NECC and the strong westward SEC (Figure 4c), but it also coincides with strong negative values of wind-stress curl (not shown).

[32] Spatio-temporal variations of the large-scale surface circulation characteristics were studied in sections 3 and 4. The turbulent part of the flow was also analyzed in terms of eddy kinetic energy. However, to further investigate the turbulence of the study region, the next section deals with its typical Lagrangian scales and eddy diffusivity coefficients.

5. Lagrangian Statistics

5.1. Single-Particle Dispersion From Taylor's (1921) Theory

[33] Lagrangian drifters are well-suited for the analysis of dispersion behavior, which can lead to improved parameterizations in circulation models and to a better understanding of lateral mixing processes in the ocean. Based on Taylor's (1921) theory, in homogeneous and stationary turbulence an estimation of the time and distance over which particles displacements are auto-correlated is given by the Lagrangian integral time and length scales (**T** and **L**, respectively) by [e.g., *Colin de Verdiere*, 1983; *Krauss and Boning*, 1987; *Haynes and Barton*, 1991]:

$$\mathbf{T} = \frac{1}{\mathbf{R}(0)} \int_0^\infty \mathbf{R}(\tau) \cdot d\tau \tag{1}$$

and

$$\mathbf{L} = \sqrt{\overline{\mathbf{u'^2}}} \cdot \mathbf{T} \tag{2}$$

where $\mathbf{R} = (R_u, R_v)$ are the Lagrangian velocity autocorrelation functions and the overbar denotes ensemble average of individual particles. In practice, as time-series have a finite length and as **R** are contaminated at large lags by noise and uncertainties in mean current, the autocorrelation functions are commonly integrated to the first zero crossing **Γ**. This corresponds to the first maximum of the integral scales and the values can be considered as upper limits for the true scales.

[34] Eddy diffusivity coefficients $\mathbf{K} = (K_u, K_v)$ are given by:

$$\mathbf{K}(t) = \overline{\mathbf{u'^2}} \int_0^t \frac{\mathbf{R}(\tau)}{\mathbf{R}(0)} \cdot d\tau \tag{3}$$

Thus, after several integral timescales **T**, corresponding to the random walk regime, the Lagrangian eddy diffusivities are expected to converge to a constant value:

$$\mathbf{K}(t) \approx \overline{\mathbf{u'^2}} \cdot T \quad \text{for } t \gg \mathbf{T} \tag{4}$$

[35] This diffusivity value can be related to the lateral mixing efficiency and is commonly used to parameterize

diffusive transports through a Fickian law [*Armi*, 1979; *Figueroa and Olson*, 1994; *Figueroa*, 1994]. Based on the integration of the velocity autocorrelation functions, the objective of the next sections is to compute the integral scales (**T** and **L**) and the eddy diffusivity coefficient (**K**) corresponding to the random walk regime. However, the Taylor (1921) dispersion theory is valid for stationary and homogeneous turbulent flow, under which the velocity departures have Gaussian probability distributions. Thus, in order to compute Lagrangian statistics in the Panama Bight and surrounding regions, we first analyse to what extent the velocity fluctuations are normally distributed.

5.2. Probability Density Functions of the Turbulent Flow and Energetic Events

[36] Inhomogeneity and nonstationarity for Lagrangian statistics have been poorly explored from satellite-tracked drifters. Several studies have however dealt with this problem in limited areas, such as in the California Current [*Swenson and Niiler*, 1996], in the Adriatic Sea [*Falco et al.*, 2000; *Maurizi et al.*, 2004], or in the Atlantic Ocean [*Bracco et al.*, 2000; *Zhang et al.*, 2001; *Colas*, 2003]. As done by these authors, we compute the probability density functions (pdfs) of the turbulent flow to test how well the mean currents are resolved and removed from the total flow. Different parameters and statistical tests are useful to determine whether a distribution is normal or not, such as the skewness $\mathbf{s} = (s_u, s_v)$, the kurtosis $\mathbf{k} = (k_u, k_v)$, or the Kolmogorov-Smirnov test.

[37] Figures 8a and 8b show the Gaussian parameters' distribution (skewness and kurtosis) of the turbulent flow as a function of bin resolution of the mean currents. For both velocity components and for resolutions lower than $\sim 0.3°$, these coefficients are nearly constant and the distributions are not normal ($\mathbf{s}_{u,v} \neq 0$ and $\mathbf{k}_{u,v} \neq 3$). The pdfs of the turbulent flow computed from mean currents obtained on $0.6° \times 0.6°$ bins (Figure 3) have maximum skewness and kurtosis of $s_u = -0.3$ and $k_u = 4.4$ respectively, suggesting that the departure from a Gaussian distribution is primarily due to an excess of infrequent energetic events [*Bracco et al.*, 2000]. Figures 8c and 8d show Lagrangian velocity pdfs normalized by the variance, where 255 (167 respectively) energetic events, in which the modulus of normalized velocity were arbitrarily chosen higher than 3.5, have been removed in the zonal (meridional) direction. Note that this criterion ($\frac{u'}{\sqrt{u'^2}} > 3.5$) was also used by *Bracco et al.* [2000] to identify energetic events in the Atlantic Ocean. The distribution parameters are now reduced and tend to more Gaussian values, particularly along the meridional direction (Figure 8d). This is confirmed by a Kolmogorov-Smirnov test at a 95% confidence level with probability values of 0.2 and ~ 1 for zonal and meridional velocity fluctuations.

[38] We could suspect that these outliers are the result of the kriging method used to interpolate the raw drifter data at 6h intervals. However, their spatial distribution (Figure 8e) shows that they are generally clumped together with swift trajectories in a single direction and most of them are longer in duration than a few days. Rather, this may be the result of coherent advection due to organized flow, since the majority of the trajectories are oriented from east to west. The westward orientation is also confirmed by strong negative skewness in the zonal direction (Figure 8a). Around 2/3 of the identified energetic events take place between 2°N–5°N and west of 82°W (Figure 8e), in the transition region between well-defined SEC and NECC (Figures 3b, 4, and 5). Interestingly, 70% of these infrequent events occur during winter months and 90% between December and April (inset of Figure 8e), which is probably associated with the westward jet observed in the SEC/NECC transition zone in winter (Figure 4a). This result suggests that the seasonal circulation, not removed to compute the turbulent flow, may be mainly responsible for the observed outliers.

[39] In order to test the possible impact of the mean current temporal variability on the turbulent velocity distributions, velocity departures are now computed relative to the seasonal circulation presented in Figure 4. Energetic events, identified previously as $\frac{u'}{\sqrt{u'^2}} > 3.5$, now represent 1.6% of the global data set and are randomly distributed over the whole study region (not shown). The NECC/SEC transition zone contains less than 25% of these infrequent events, which roughly corresponds to the ratio of its area to the global oceanic study region. Each month of the year now contains between 4% and 17% of the outliers. Table 3 shows the Gaussian parameters of the normalized velocity pdfs indicating the excellent agreement with normal distributions ($s_{u,v} < 0.07$, $k_{u,v} = 2.9$, $p = 1$). This suggests that temporal fluctuation of the mean flow has strong influence on the velocity departure distributions and that the seasonal cycle may be removed to correctly compute Lagrangian scales and eddy diffusivity coefficients from velocity autocorrelation functions. Gaussian parameters of the pdfs, computed in both sub-regions without previously identified energetic events are shown in Table 3. Based on these values ($0 < s_{u,v} < 0.06$, $2.8 < k_{u,v} < 3$ and $0.97 < p_{u,v} < 1$), the turbulence in the NECC, PBCG and SEC regions can be considered as homogeneous and stationary. Thus, Taylor's (1921) theory may be applied to these distributions for the computation of Lagrangian scales and lateral eddy diffusivities.

5.3. Autocorrelation Functions

[40] The Lagrangian autocovariance functions **R** were computed for each drifter spending more than 10 days in the domain and then ensemble averaged. To increase the number of degrees of freedom, the trajectories were previously reinitialized every 10 days (this value is much longer than the 1–4 days Lagrangian timescales, see below), as done in different studies [*Colin de Verdiere*, 1983; *Poulain and Niiler*, 1989; *Haynes and Barton*, 1991; *Martins et al.*, 2002; *Chaigneau and Pizarro*, 2005]. The mean autocorrelation functions of both velocity components, computed from 973 trajectories assumed to be independent, are shown in Figure 9. Standard errors (gray shading), computed as a Student's *t* test with a significance level of 5%, are weak and of the order of 1%.

[41] The zonal autocorrelation function R_u for the whole study region (Figure 9a) is characterized by two different regimes with approximately exponential behavior. For small lags ($t < 2$ days), it presents an e-folding scale of around 2 days, whereas for longer lags ($t > 4$ days) a second exponential behavior is observed with a decay time of ~ 8 days. The short timescale may be principally

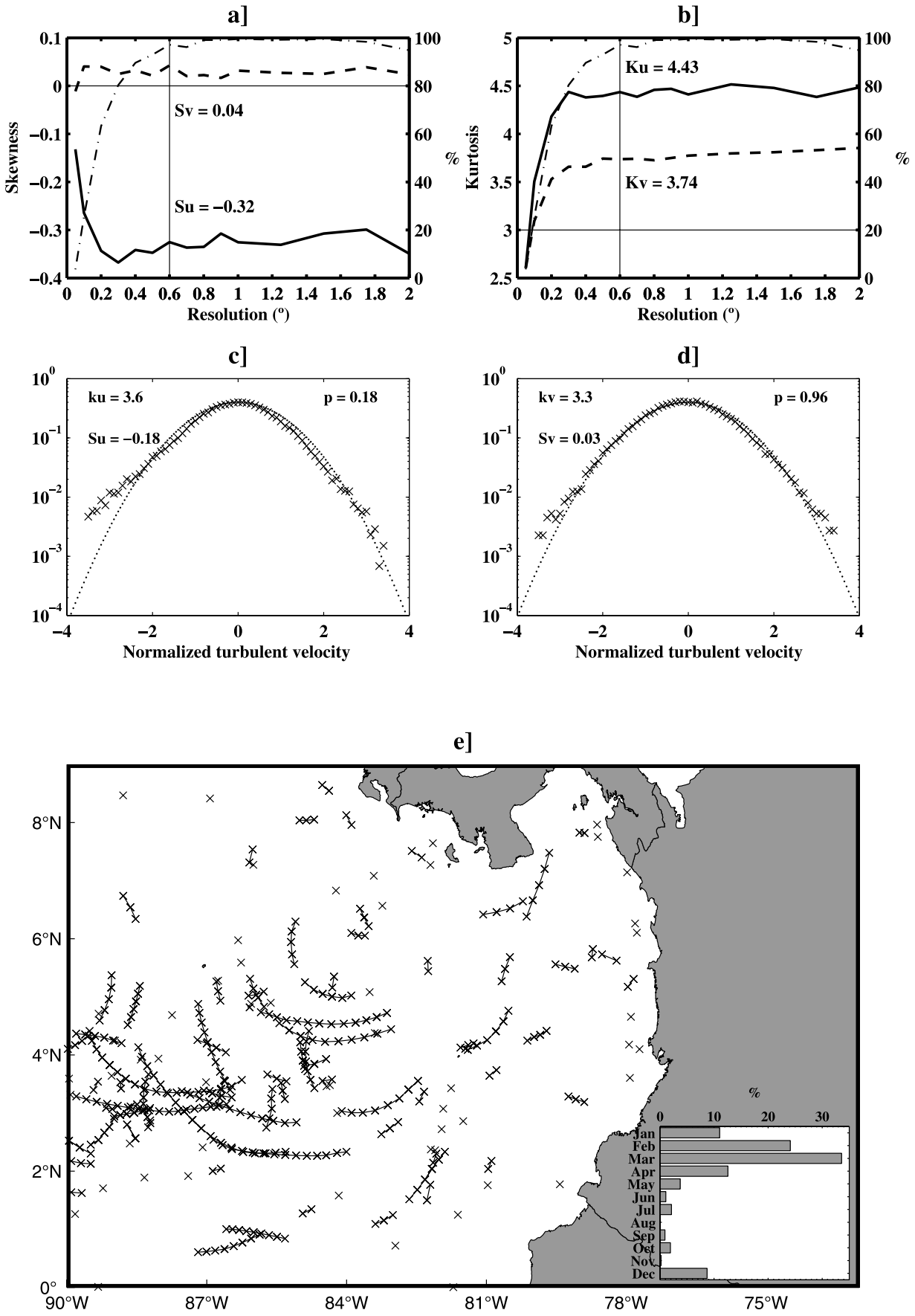
a]
Skewness
%
Sv = 0.04
Su = −0.32
Resolution (°)
b]
Kurtosis
%
Ku = 4.43
Kv = 3.74
Resolution (°)
c]
ku = 3.6
p = 0.18
Su = −0.18
Normalized turbulent velocity
d]
kv = 3.3
p = 0.96
Sv = 0.03
Normalized turbulent velocity
e]
8°N
6°N
4°N
2°N
0°
90°W
87°W
84°W
81°W
78°W
75°W
%
Jan
Feb
Mar
Apr
May
Jun
Jul
Aug
Sep
Oct
Nov
Dec

Figure 8

Table 3. Gaussian Parameters and Number of Infrequent Energetic Events Computed From Probability Density Functions of Normalized Velocity Departures Without Energetic Events

	Skewness		Kurtosis		KS-Test		Energetic Events	
	s_u	s_v	k_u	k_v	p_u	p_v	n_u	n_v
Global Region	0.07	0.02	2.9	2.9	1.00	1.00	794	382
NECC Region	0.11	0.00	2.9	2.9	0.99	1.00	235	101
PBCG Region	0.02	0.03	2.9	3.0	1.00	0.97	114	159
SEC Region	0.02	0.06	3.0	2.8	1.00	1.00	445	122

associated with mesoscale activity and direct wind forcing, whereas the longer timescale could be related to other processes such as long-lived coherent eddies, near-equatorial long wave dynamics, or low-frequency fluctuations of the circulation [see *Maurizi et al.*, 2004]. In contrast, R_v presents an e-folding scale of ~1.5 days and even if a weak secondary maximum is observed at a lag of ~5 days, R_v converges more rapidly to zero. The zonal scales are much higher than their meridional counterparts and therefore could probably be induced by turbulent fluctuations linked to mean current instabilities, since these instabilities tend to develop structures in the direction of the mean currents (mostly zonal in our case) [*Maurizi et al.*, 2004]. Thus, the zonal dispersion may be dominated by coherent long-lived structures, whereas meridional dispersion is faster and may be dominated by a diffuse regime.

[42] The autocorrelation functions show distinct characteristics in the three sub-regions (Figure 9b). In the NECC region, both R_u and R_v show a local maximum at a lag of 4–5 days and have large first zero crossings of ~20 days and ~7 days, respectively. These secondary maxima (or "knees") are generally caused by inertial motions [*Bauer et al.*, 1998, 2002]. The NECC region spans latitudes 3°N–9°N, corresponding to large inertial periods of ~3–9 days which result in broad correlation in $R_{u,v}$. The anisotropy observed in the NECC region, with an elongation in the zonal direction due to the mean eastward currents, is reduced in the Panama Bight because of the near circular circulation. In this region, R_u and R_v are tightly grouped and have a similar first zero crossing of 7–8 days. However, the influence of inertial motions is also visible in the PBCG with slight secondary maxima at a lag of ~5 days. Finally in the SEC region, R_u decreases in a near-exponential way with an e-folding scale of 2.5 days and a first-zero crossing of ~15 days, whereas R_v converges rapidly to zero after vanishing at a lag of ~4 days. In this region, no inertial oscillation correlation is observed because Coriolis effects are less important near the equatorial band. The R_v comportment in this region can be interpreted as the signature of tropical instability waves [*Bauer et al.*, 1998, 2002] which have been observed east of 90°W [*Chelton et al.*, 2000b, Plate 5; *Yu and Liu*, 2003, Figure 3].

5.4. Estimates of the Lagrangian Scales and Diffusivity Coefficients

[43] Estimates of the Lagrangian scales (**T** and **L**) and of the lateral diffusivity coefficients (**K**) are computed through the integration of the mean autocorrelation functions to their first zero crossing Γ (equations (1)–(4)). Their mean values and the associated standard errors at a 95% confidence level are given in Table 4. No significant difference is observed between the whole study domain and the NECC region. Strong elongation in the zonal direction is again observed with zonal parameters being around 2 times larger than their meridional counterparts. In the PBCG region, all the computed parameters are reduced by a factor of two in the zonal direction leading to an almost isotropic diffusivity in this region. In the SEC region, we observe large parameter values in the zonal direction and smaller ones in the meridional direction, due to a faster convergence of R_v (Figure 9) and lower kinetic energy (Table 4).

[44] Except in the PBCG region, the zonal timescales are higher than the e-folding scales of ~2 days previously determined, again indicating the influence of the different co-existing dynamic processes in the zonal direction. In contrast in the meridional direction, Lagrangian timescales of 1.4–1.8 days are in the range of the e-folding scale representative of a diffuse regime. Lagrangian length scales also reveal the anisotropic nature of the dispersion processes in the NECC and SEC regions with typical values of 50–65 km along the zonal direction and 20–30 km along the meridional direction. The PBCG shows isotropic length scales of 30 km. The estimates of $\boldsymbol{L}$ from drifter data in the Black Sea [*Zhurbas et al.*, 2004], together with similar estimates for the Adriatic Sea [*Falco et al.*, 2000], the Sea of Japan and the northwestern part of the Pacific Ocean [*Oh et al.*, 2000], fit the relation $\boldsymbol{L} = R_d$, where R_d is the internal Rossby radius of deformation. In contrast in the study region, the observed scales of the turbulence (<65 km) are lower than the typical baroclinic Rossby radii which are larger than 150 km south of 10°N [*Chelton et al.*, 1998].

[45] In the NECC and SEC regions the combination of higher energy levels and larger timescales in the zonal direction (Table 4) give large diffusivity coefficients K_u in the order of 10–15 10^7 cm^2 s^{-1}. In the PBCG, K_u only reaches a value of ~6 10^7 cm^2 s^{-1}, similar to the meridional

Figure 8. Binned (a) skewness and (b) kurtosis in Cartesian coordinates (u = zonal, in solid lines and v = meridional, in dashed lines) computed over the study region as function of squared bin resolution. Also indicated (dotted dashed line) is the percentage of independent data used in the estimates, as the ratio of data belonging to significant bins and total number of data (65 656). (c) Zonal and (d) meridional probability density functions of normalized velocity departures from the annual mean circulation, without energetic events (see text for definition). Skewness ($s_{u,v}$), kurtosis ($k_{u,v}$) and p-values (p) of the statistical Kolmogorov-Smirnov test are also indicated. (e) Spatial distribution of the infrequent energetic events; the inset represents their monthly distribution (in %).

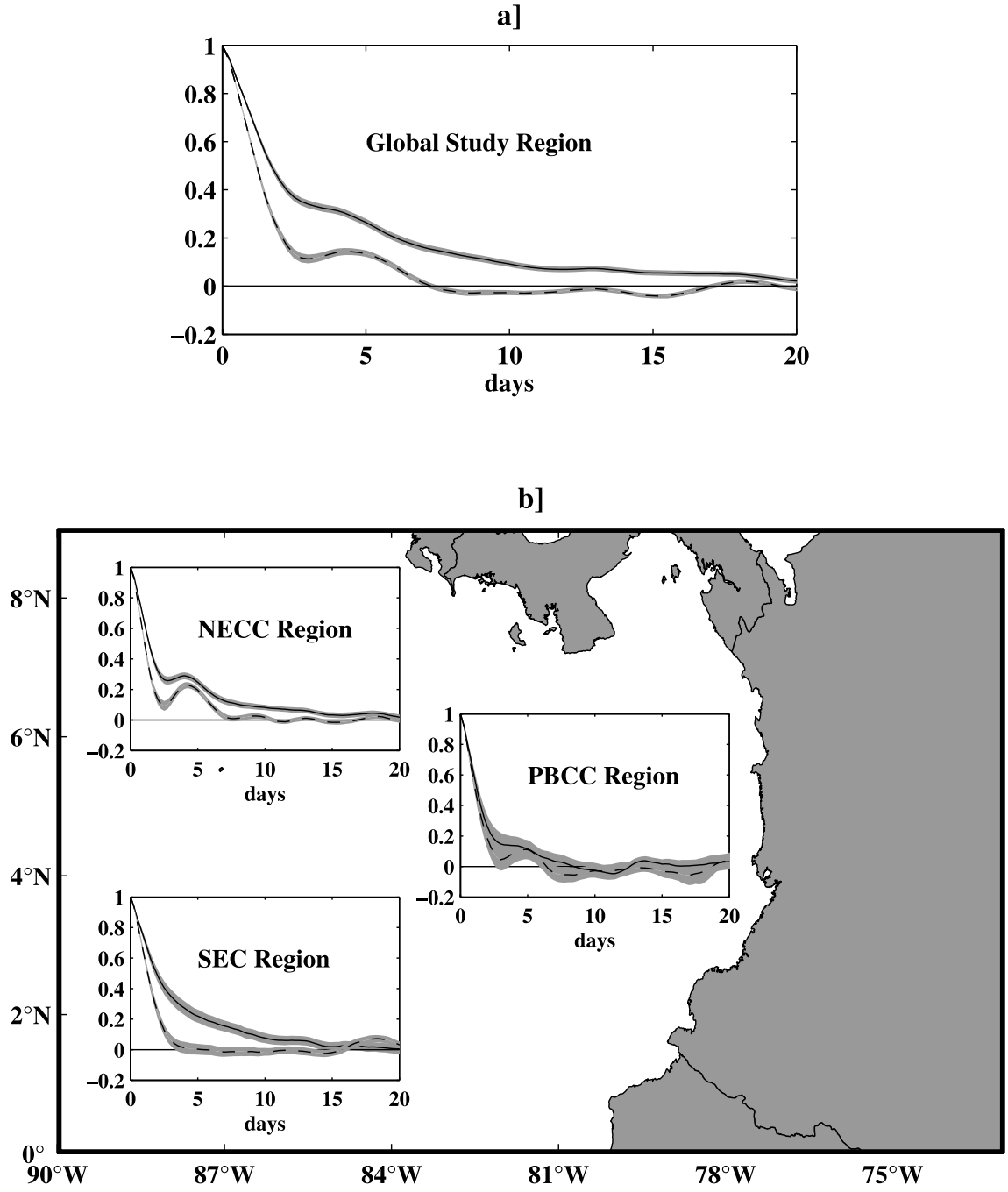

Figure 9. Temporal evolution of the normalized velocity autocorrelation functions. (a) whole study region and (b) NECC, PBCG and SEC regions. These were computed from zonal (solid lines) and meridional (dashed lines) velocity departures, relative to the seasonal circulation. The infrequent energetic events, as defined in the text, were previously removed.

coefficients observed in both the NECC and SEC regions. It should be noted that the calculated diffusivities might be relatively large since they also include the tidal and inertial current components which may modify the eddy diffusivity. These estimates (Table 4) should be considered with caution since Taylor's (1921) theory is valid in homogeneous turbulence in the absence of waves or coherent structures. In particular, meridional scales of the SEC region could be underestimated due to the presence of tropical instability waves which could possibly explain the rapid decrease of the velocity autocorrelation function R_v (see section 5.3).

6. Summary and Conclusions

[46] The goal of this study was to describe the mean surface circulation and the turbulent characteristics of the flow in the Panama Bight and surrounding regions. On the basis of high-coverage data from satellite-tracked drifters deployed throughout the 1979–2004 period, large-scale

Table 4. Velocity Variances, Lagrangian Timescales and Length Scales, and Eddy Diffusivity Coefficients for Zonal and Meridional Directions

	Variance, $cm^2\ s^{-2}$		Timescales, days		Length Scales, km		Diffusivity, $10^7\ cm^2\ s^{-1}$	
	$\overline{u'^2}$	$\overline{v'^2}$	T_u	T_v	L_u	L_v	K_u	K_v
Global Region	532.0	418.5	3.2 ± 0.4	1.7 ± 0.1	63.5 ± 8.9	29.3 ± 1.5	14.6 ± 2.0	6.0 ± 0.3
NECC Region	592.0	453.7	2.7 ± 0.4	1.6 ± 0.1	56.2 ± 8.1	29.6 ± 2.7	13.7 ± 2.0	6.3 ± 0.6
PBCG Region	447.6	385.9	1.6 ± 0.3	1.8 ± 0.2	29.3 ± 4.6	30.0 ± 3.7	6.2 ± 1.0	5.9 ± 0.7
SEC Region	473.6	370.1	2.7 ± 0.5	1.4 ± 0.1	51.3 ± 9.8	23.3 ± 2.4	11.2 ± 2.1	4.5 ± 0.5

current features were quantitatively analyzed in this region. Three main currents were studied: (1) the eastward North Equatorial Counter Current (NECC) centred at ~7°S; (2) the Panama Bight Cyclonic Gyre (PBCG); and (3) the westward South Equatorial Current (SEC). These three main currents exhibit typical mean surface velocities in the order of 30 cm s^{-1}.

[47] At interannual scales during ENSO events, the data analysis does not show significant changes in the mean regional circulation and kinematic properties such as kinetic energy levels or large-scale relative vorticity. However, we observed a slight strengthened of the SEC during relatively warm El Niño periods. This result, although in contradiction to what is generally observed in the central and western tropical Pacific, confirms what was noted at 95°W from hydrographic measurements during the strong ENSO events of the 1990s [*Johnson et al.*, 2000, 2002; *Grodsky and Carton*, 2001].

[48] At seasonal scales, the near-surface circulation variability is controlled mainly by the winds regime. In winter, an anticyclonic cell is observed west of the persistent PBCG, forced directly by the Panama jet blowing during this season and by its associated curl. This dipolar circulation (anticyclonic at the west/cyclonic at the east) produces a strong southwestward jet of 200 km width, where speeds higher than 50 cm s^{-1} are commonly observed. Both the NECC and PBCG are reinforced in winter and spring and weakened in summer and fall. In contrast, the SEC exhibits a semiannual cycle with maximum eastward velocities in winter and summer. In the main part of the study region, the mean kinetic energy (MKE) is weak compared to the eddy kinetic energy (EKE). Higher values of EKE are found in the central region where the zonal shear induced by the winter dipolar circulation is favorable to eddy activity. This area is also subject seasonally to the Panama wind jet which enhances the eddy activity of the upper layer. Total kinetic energy is twice as high in winter than during summer and fall. The relative vorticity associated with the large-scale circulation also shows significant seasonal-changes: for example, the upwelling associated with the PBCG is 3–4 times stronger during winter than during summer.

[49] When seasonal cycle is removed from the mean circulation, the pdfs of the velocity departures are Gaussian. In this homogeneous and stationary turbulence, the classical Taylor (1921) theory was applied to compute Lagrangian characteristics and eddy diffusivity coefficients. These parameters are important since they help to characterize the turbulence and to validate the parameterization of the lateral mixing. Anisotropy with higher Lagrangian scales along the zonal direction was observed in the NECC and SEC regions where the mean circulations are predominantly oriented eastward and westward respectively. The typical timescales (length scales, respectively) in these regions are of order of 2.5 days (50–60 km) in the zonal direction and 1.5 days (25–30 km) in the meridional direction. Lateral diffusivities are of the order of 11–14 $10^7\ cm^2\ s^{-1}$ zonally and 5–6 $10^7\ cm^2\ s^{-1}$ meridionally. In contrast, Lagrangian scales related to the near-circular circulation of the PBCG are isotropic, with typical timescales of 1.7 days, space scales of 30 km and eddy diffusivity coefficients of 6 $10^7\ cm^2\ s^{-1}$ in both directions. As was also observed in the tropical Pacific Ocean [*Bauer et al.*, 1998, 2002], inertial motions and instability waves appear to affect the velocity autocorrelation functions and may slightly bias the estimated Lagrangian scales and horizontal diffusivity coefficients. However, our estimates are an order of magnitude lower than the results of these authors, who found for example values of K_u reaching 25 $10^7\ cm^2\ s^{-1}$ in a region encompassing the NECC flow (4°N–10°N and 160°W–100°W) and 73 $10^7\ cm^2\ s^{-1}$ in a region encompassing the SEC (3°S–3°N and 150°W–100°W). These differences may probably be attributed to a stronger tropical instability wave activity west of 90°W [*Chelton et al.*, 2000b], leading to an increase in the velocity variance and hence to higher diffusivity values. The Lagrangian scales and lateral mixing coefficients of the Panama Bight and surrounding regions are in contrast higher than in the eastern boundary currents such as the California Current in the North Pacific [*Swenson and Niiler*, 1996] or the Peru-Chile Current in the South-Pacific [*Chaigneau and Pizarro*, 2005], principally due to higher velocity variance in the tropical regions.

[50] We have investigated the mean surface circulation and turbulent flow characteristics of the eastern part of the tropical Pacific around the Panama Bight. In this poorly sampled region, more satellite-tracked drifters and in situ measurements are required to better resolve the temporal fluctuations at intraseasonal scales. The results obtained here could provide useful information for validating regional numerical models. A future work will be devoted to the estimation of lateral heat and salt fluxes across the study region using lateral mixing coefficients previously determined.

Appendix A: Standard Errors, Slip of the Drogue, Positioning Errors, and Array Bias

[51] The mean flow estimated from drifter measurements is expected to be affected by sampling errors due to the finite number of observations and due to the subscale variability. The statistical uncertainty (ΔQ), or standard error on the mean quantity Q (e.g., velocity components U, V), was evaluated using Student's t test with a significance level of 5%:

$$\Delta Q = t_{N-1,0.025}\frac{\sigma_Q}{\sqrt{N*}}$$

where σ_Q represents the standard deviation and N^* is the number of independent observations. The factor $t_{N-1,0.025}$, $2 > t_{N-1,0.025} > 1.96$ for $N^* > 60$, leads to maximum standard errors. The sampling error is generally represented by displaying a 95% confidence ellipse around the mean flow vector (see section 3). This ellipse has the same orientation as the velocity variance ellipse and its principal axes are given by [*Emery and Thomson*, 1998]:

$$\text{Semimajor (minor) axis} \approx 2\sqrt{\frac{\lambda_{1,2}}{N^*}}$$

where $\lambda_{1,2}$ are the two eigenvalues of the velocity covariance matrix.

[52] In addition to the uncertainty of the sample mean, errors may arise due to external factors such as relative wind-slips of the drogue [*Niiler and Paduan*, 1995], positioning errors from ARGOS fixing, or from the spatio-temporal heterogeneity of the float concentration [*Davis*, 1991]. With commonly achieved drifter position accuracy of 150–300 m and time intervals of 6 h between successive interpolated positions, the velocity errors are less than 1.5 cm s^{-1}. These errors are random so their net effect on the velocity estimates are small compared to the 10–150 cm s^{-1} currents typically observed in the surface layer of the region. Because surface drifters are designed to have a large drogue to non-drogue drag ratio, velocity errors arising from wind drag and from slippage between the water and the drogue are expected to be smaller than 2 cm s^{-1} for winds up to 20 m s^{-1} [*Niiler and Paduan*, 1995]. Using daily distributed wind fields from Quikscat satellite measurements (http://podaac.jpl.nasa.gov/poet), the maximum wind speed observed in the study region was of the order of 15 m s^{-1} and on average about 5 m s^{-1}. Thus, relative wind-induced slip may be less than 1–2 cm s^{-1} for the conditions expected to be encountered. Finally, *Davis* [1991] pointed out that heterogeneity of the drifter deployments may drive a "diffuse" flux of floats away from well-sampled regions. This array bias which contaminates the estimate of mean velocity of up to few cm s^{-1} was estimated as:

$$U_{array} = -\mathbf{K} \cdot \nabla \ln C$$

where $\boldsymbol{K} = (K_x, K_y)$ are the zonal and meridional eddy diffusivity coefficients given in Table 4 and C the drifter concentration per unit area. The computed array bias (not shown) is on average of the order of 4.8 cm s^{-1} in the NECC and SEC regions and of 3.6 cm s^{-1} in the PBCG region. Across the majority of the three sub-regions, the magnitude of array bias is thus smaller than the estimated sampling errors (Figures 3–5).

[53] **Acknowledgments.** We especially thank G. Reverdin for his precious comments and A. Thom for her sugestions. We also thank B. Lagos from the Statistics Department of the University of Concepción for his help in statistical errors computation. The Quikscat winds were obtained from the Physical Oceanography Distributed Active Archive Center (PO.DAAC) at the NASA Jet Propulsion Laboratory, Pasadena, California.

References

Alfaro, E. J. (2000), Some characteristics of the precipitation annual cycle in Central America and their relationships with its surrounding tropical oceans, *Top. Meteorol. Oceanogr.*, *7*(2), 99–115.

Alford, M. H. (2003), Improved global maps and 54-year history of wind-work on ocean inertial motions, *Geophys. Res. Lett.*, *30*(8), 1424, doi:10.1029/2002GL016614.

Armi, L. (1979), Effects of variations in eddy diffusivity on property distributions in the ocean, *J. Mar. Res.*, *37*(3), 515–530.

Ballance, L. T., R. L. Pitman, and S. B. Reilly (1997), Seabird community structure along a productivity gradient: Importance of competition and energetic constraint, *Ecology*, *78*(5), 1502–1518.

Bauer, S., M. S. Swenson, A. Griffa, A. J. Mariano, and K. Owens (1998), Eddy mean flow decomposition and eddy diffusivity estimates in the tropical Pacific Ocean: 1. Methodology, *J. Geophys. Res.*, *103*(C13), 30,855–30,871.

Bauer, S., M. S. Swenson, and A. Griffa (2002), Eddy mean flow decomposition and eddy diffusivity estimates in the tropical Pacific Ocean: 2. Results, *J. Geophys. Res.*, *107*(C10), 3154, doi:10.1029/2000JC000613.

Bracco, A., J. H. LaCasce, and A. Provenzale (2000), Velocity probability density functions for oceanic floats, *J. Phys. Oceanogr.*, *30*, 461–474.

Brugge, B. (1995), Near-surface mean circulation and kinetic energy in the central North Atlantic from drifter data, *J. Geophys. Res.*, *100*(C10), 10,543–10,554.

Bryden, H. L., and E. C. Brady (1989), Eddy momentum and heat fluxes and their effects on the circulation of the equatorial Pacific Ocean, *J. Mar. Res.*, *47*, 55–79.

Carr, M. E., and H. T. Rossby (2001), Pathways of the North Atlantic Current from surface drifters and subsurface floats, *J. Geophys. Res.*, *106*(C3), 4405–4419.

Chaigneau, A., and O. Pizarro (2005), Mean surface circulation and mesoscale turbulent flow characteristics in the eastern South Pacific from satellite tracked drifters, *J. Geophys. Res.*, *110*, C05014, doi:10.1029/2004JC002628.

Chavez, F. P., P. G. Strutton, G. E. Friederich, R. A. Feely, G. C. Feldman, D. G. Foley, and M. J. McPhaden (1999), Biological and chemical response of the equatorial Pacific ocean to the 1997–98 El Niño, *Science*, *286*, 2126–2131.

Chelton, D. B. (2000), Satellite observations of the wind jets off the Pacific Coast of Central America. Part II: Relationships and dynamical considerations, *Mon. Weather Rev.*, *128*, 2019–2043.

Chelton, D. B., R. A. deSzoeke, M. G. Schlax, K. El Naggar, and N. Siwertz (1998), Geographical variability of the first-baroclinic Rossby radius of deformation, *J. Phys. Oceanogr.*, *28*, 433–460.

Chelton, D. B., M. H. Freilich, and S. K. Esbensen (2000a), Satellite observations of the wind jets off the Pacific coast of Central America. Part I: Case studies and statistical characteristics, *Mon. Weather Rev.*, *128*, 1993–2018.

Chelton, D. B., F. J. Wentz, C. L. Gentemann, R. A. De Szoeke, and M. G. Schlax (2000b), Satellite microwave SST observations of transequatorial tropical instability waves, *Geophys. Res. Lett.*, *27*, 1239–1242.

Colas, F. (2003), Circulation et dispersion Lagrangienne en Atlantique Nord-Est, thèse de 3ème cycle, 261 pp., Univ. de Bretagne Occident.

Colin de Verdiere, A. (1983), Lagrangian eddy statistics from surface drifters in the eastern north Atlantic, *J. Mar. Res.*, *41*, 375–398.

Cronin, M. F., and W. S. Kessler (2002), Seasonal and interannual modulation of mixed layer variability at 0°, 110°W, *Deep Sea Res., Part I*, *49*, 1–17.

Davis, R. E. (1991), Observing the general circulation with floats, *Deep Sea Res.*, *38*, S531–S571.

Ducet, N., P. Y. Le Traon, and G. Reverdin (2000), Global high-resolution mapping of ocean circulation from TOPEX/Poseidon and ERS-1 and -2, *J. Geophys. Res.*, *105*(C8), 19,477–19,498.

Emery, W. J., and R. E. Thomson (1998), *Data Analysis Methods in Physical Oceanography*, 634 pp., Elsevier, New York.

Enfield, D. B. (1996), Relationships of inter-American rainfall to tropical Atlantic and Pacific SST variability, *Geophys. Res. Lett.*, *23*(23), 3305–3308.

Enfield, D. B., and E. J. Alfaro (1999), The dependence of Caribbean rainfall on the interaction of the tropical Atlantic and Pacific oceans, *J. Clim.*, *2*, 2093–2103.

Falco, P., A. Griffa, P.-M. Poulain, and E. Zambianchi (2000), Transport properties in the Adriatic Sea as deduced from drifter data, *J. Phys. Oceanogr.*, *30*, 2055–2071.

Fiedler, P. C. (1999), Eastern Tropical Pacific dolphins habitat variability, report to Congress of International Dolphin Conservation Program Act, draft report, 11 pp., Southwest Fish. Sci. Cent.

Fiedler, P. C. (2002a), The annual cycle and biological effects of the Costa Rica Dome, *Deep Sea Res., Part I*, *49*, 321–338.

Fiedler, P. C. (2002b), Environmental change in the eastern tropical Pacific Ocean: Review of ENSO and decadal variability, *Mar. Ecol. Prog. Ser.*, *44*, 265–283.

Figueroa, H. A. (1994), Eddy resolution versus eddy diffusion in a double gyre GCM. Part II: Mixing of passive tracers, *J. Phys. Oceanogr.*, *24*, 387–402.

Figueroa, H. A., and D. B. Olson (1994), Eddy resolution versus eddy diffusion in a double gyre GCM. Part I: The Lagrangian and Eulerian description, *J. Phys. Oceanogr.*, *24*, 371–386.

Flierl, G. R., and J. C. McWilliams (1977), On the sampling requirements for measuring moments of eddy variability, *J. Mar. Res.*, *35*, 797–820.

Grodsky, S. A., and J. A. Carton (2001), Intense surface currents in the tropical Pacific during 1996–1998, *J. Geophys. Res.*, *106*(C8), 16,673–16,684.

Gu, D., S. G. H. Pilander, and M. J. McPhaden (1997), The seasonal cycle and its modulation in the Eastern Tropical Pacific Ocean, *J. Phys. Oceanogr.*, *27*(10), 2209–2218.

Hansen, D. V., and P.-M. Poulain (1996), Quality control and interpolations of WOCE-TOGA drifter data, *J. Atmos. Oceanic Technol.*, *13*, 900–909.

Haynes, R., and E. D. Barton (1991), Lagrangian observations in the Iberian coastal transition zone, *J. Geophys. Res.*, *96*, 14,731–14,741.

Jayne, S. R., and J. Marotzke (2002), The oceanic eddy heat transport, *J. Phys. Oceanogr.*, *32*, 3328–3345.

Jiang, J., Y. Lu, and W. Perrie (2005), Estimating the energy flux from wind to ocean inertial motions: The sensitivity to surface wind fields, *Geophys. Res. Lett.*, *32*, L15610, doi:10.1029/2005GL023289.

Johnson, G. C., M. J. McPhaden, G. D. Rowe, and K. E. McTaggart (2000), Upper equatorial Pacific Ocean current and salinity variability during the 1996–1998 El Niño – La Niña cycle, *J. Geophys. Res.*, *105*(C1), 1037–1053.

Johnson, G. C., B. M. Sloyan, W. S. Kessler, and K. E. McTaggart (2002), Direct measurements of upper ocean currents and water properties across the tropical Pacific during the 1990s, *Prog. Oceanogr.*, *52*, 31–61.

Kessler, W. S. (2002), Mean three-dimensional circulation in the Northeast Tropical Pacific, *J. Phys. Oceanogr.*, *32*, 2457–2471.

Kessler, W. S. (2006), The circulation of the Eastern Tropical Pacific: A review, *Prog. Oceanogr.*, *69*, 181–217.

Kessler, W. S., and M. J. McPhaden (1995), Oceanic equatorial waves and the 1991–93 El Niño, *J. Clim.*, *8*, 1757–1774.

Krauss, W., and C. W. Boning (1987), Lagrangian properties of eddy fields in the northern Atlantic as deduced from satellite-tracked buoys, *J. Mar. Res.*, *45*, 259–291.

Le Traon, P.-Y., and R. Morrow (2001), Ocean currents and eddies, in *Satellite Altimetry and Earth Sciences: A Handbook of Techniques and Applications*, edited by L.-L. Fu and A. Cazenave, 457 pp., Elsevier, New York.

Loubere, P. (2000), Marine control of biological production in the eastern equatorial Pacific, *Nature*, *406*, 497–500.

Martins, C. S., M. Hamann, and A. F. G. Fiúza (2002), Surface circulation in the eastern North Atlantic, from drifters and altimetry, *J. Geophys. Res.*, *107*(C12), 3217, doi:10.1029/2000JC000345.

Maurizi, A., A. Griffa, P.-M. Poulain, and F. Tampieri (2004), Lagrangian turbulence in the Adriatic Sea as computed from drifter data: Effects of inhomogeneity and nonstationarity, *J. Geophys. Res.*, *109*, C04010, doi:10.1029/2003JC002119.

McCreary, J. P., H. S. Lee, and D. B. Enfield (1989), The response of the coastal ocean to strong offshore winds: With application to circulations in the Gulfs of Tehuantepec and Papagayo, *J. Mar. Res.*, *47*, 81–109.

McGillicuddy, D. J., A. R. Robinson, D. A. Siegel, H. W. Jannasch, R. Johnson, T. D. Dickey, J. D. McNeil, A. F. Michaels, and A. H. Knap (1998), New evidence for the impact of mesoscale eddies on biogeochemical cycling in the Sargasso Sea, *Nature*, *394*, 263–266.

Morrow, R., R. Coleman, J. Church, and D. Chelton (1994), Surface eddy momentum flux and velocity variances in the Southern Ocean from Geosat altimetry, *J. Phys. Oceanogr.*, *24*, 2050–2071.

Niiler, P. P. (2001), The world ocean surface circulation, in *Ocean Circulation and Climate: Observing and Modelling the Global Ocean*, *Int. Geophys. Ser.*, vol. 77, edited by G. Siedler, J. Church, and J. Gould, pp. 193–204, Elsevier, New York.

Niiler, P. P., and J. D. Paduan (1995), Wind-driven motions in the northeast Pacific as measured by Lagrangian drifters, *J. Phys. Oceanogr.*, *25*, 2819–2830.

Niiler, P. P., R. E. Davis, and H. J. White (1987), Water-following characteristics of a mixed layer drifter, *Deep Sea Res.*, *34*, 1876–1881.

Niiler, P. P., A. Sybrandy, K. Bi, P.-M. Poulain, and D. Bitterman (1995), Measurements of the water-following capability of Holey-sock and TRISTAR drifters, *Deep Sea Res.*, *42*, 1951–1964.

Niwa, Y., and T. Hibiya (2001), Numerical study of the spatial distribution of the M2 internal tide in the Pacific Ocean, *J. Geophys. Res.*, *106*(C10), 22,441–22,449.

Oh, I. S., V. M. Zhurbas, and W. S. Park (2000), Estimating horizontal diffusivity in the East Sea (Sea of Japan) and the Northwest Pacific from satellite-tracked drifter data, *J. Geophys. Res.*, *105*(C3), 6483–6492.

Palacios, D. M. (2004), Seasonal patterns of sea surface temperature and ocean color around the Galapagos: Regional and local influences, *Deep Sea Res., Part II*, *51*, 43–57.

Philander, S. G. (1990), *El Niño, La Niña and the Southern Oscillation*, *Int. Geophys. Ser.*, vol. 46, 294 pp., Elsevier, New York.

Poulain, P.-M., and P. P. Niiler (1989), Statistical analysis of the surface circulation in the California Current system using satellite-tracked drifters, *J. Phys. Oceanogr.*, *19*, 1588–1603.

Poulain, P. P. (2001), Adriatic Sea surface circulation as derived from drifter data from 1990 and 1999, *J. Mar. Syst.*, *29*, 3–32.

Ralph, E. A., and P. P. Niiler (1999), Wind-driven currents in the Tropical Pacific, *J. Phys. Oceanogr.*, *29*, 2121–2129.

Ray, R. D., and G. D. Egbert (2004), The global S1 tide, *J. Phys. Oceanogr.*, *34*, 1922–1935.

Reverdin, G., C. Frankignoul, E. Kastenare, and M. J. McPhaden (1994), Seasonal variability in the surface currents of the equatorial Pacific, *J. Geophys. Res.*, *99*(C10), 20,323–20,344.

Rodríguez-Rubio, E., and J. Stuardo (2002), Variability of photosynthetic pigments in the Colombian Pacific Ocean and its relationship with the wind field using ADEOS-I data, *Earth Planet. Sci.*, *111*(3), 227–236.

Rodríguez-Rubio, E., W. Schneider, and A. Abarca del Rio (2003), On the seasonal circulation within the Panama Bight derived from satellite observations of wind, altimetry and sea-surface temperature, *Geophys. Res. Lett.*, *30*(7), 1410, doi:10.1029/2002GL016794.

Spear, L. B., L. T. Balance, and D. G. Ainley (2001), Response of seabirds to thermal boundaries in the tropical Pacific: The thermocline versus the Equatorial Front, *Mar. Ecol. Prog. Ser.*, *219*, 275–289.

Stevenson, M. (1970), Circulation in the Panama Bight, *J. Geophys. Res.*, *75*, 659–672.

Swenson, M. S., and P. P. Niiler (1996), Statistical analysis of the surface circulation of the California Current, *J. Geophys. Res.*, *101*, 22,631–22,645.

Sybrandy, A. L., and P. P. Niiler (1991), WOCE/TOGA Lagrangian drifter construction manual, *WOCE Rep. 63, SOI Ref. 91/6*, 58 pp., Scripps Inst. of Oceanogr., La Jolla, Calif.

Tans, P., I. Fung, and T. Takahashi (1990), Observational constraints on the global atmosphere CO_2 budget, *Science*, *247*, 1431–1438.

Taylor, M. A., D. B. Enfield, and A. A. Chen (2002), Influence of the tropical Atlantic versus the tropical Pacific on Caribbean rainfall, *J. Geophys. Res.*, *107*(C9), 3127, doi:10.1029/2001JC001097.

Tomczak, M., and J. S. Godfrey (1994), *Regional Oceanography: An Introduction*, 442 pp., Elsevier, New York.

Trasviña, A., E. D. Barton, J. Brown, H. S. Velez, P. M. Kosro, and R. L. Smith (1995), Offshore wind forcing in the Gulf of Tehuantepec, Mexico: The asymmetric circulation, *J. Geophys. Res.*, *100*, 20,649–20,663.

Trenberth, K. E. (1997), The definition of El Niño, *Bull. Am. Meteorol. Soc.*, *78*(12), 2771–2777.

Van Haren, H., L. St. Laurent, and D. Marshall (2004), Small and mesoscale processes and their impact on the large scale: An introduction, *Deep Sea Res., Part II*, *51*, 2883–2887.

Wooster, W. (1959), Oceanographic observations in the Panama Bight, "ASKOY" expedition, 1941, *Bull. Am. Mus. Nat. Hist.*, *118*(3), 113–152.

Xie, S. P., H. Xu, W. Kessler, and M. Nonaka (2005), Air-sea interaction over the Eastern Pacific warm pool: Gap winds, thermocline dome and atmospheric convection, *J. Clim.*, *18*(1), 5–20.

Yu, J. Y., and W. T. Liu (2003), A linear relationship between ENSO intensity and tropical instability wave activity in the eastern Pacific ocean, *Geophys. Res. Lett.*, *30*(14), 1735, doi:10.1029/2003GL017176.

Yu, X., and M. J. McPhaden (1999), Seasonal variability in the Equatorial Pacific, *J. Phys. Oceanogr.*, *29*, 925–947.

Yuan, D. (2005), Role of the Kelvin and Rossby waves in the seasonal cycle of the equatorial Pacific Ocean circulation, *J. Geophys. Res.*, *110*, C04004, doi:10.1029/2004JC002344.

Zhang, H. M., M. D. Prater, and T. Rossby (2001), Isopycnal Lagrangian statistics from the North Atlantic Current RAFOS float observations, *J. Geophys. Res.*, *106*(C7), 13,817–13,836.

Zhurbas, V. M., A. G. Zatsepin, Y. V. Grigor'eva, V. N. Eremeev, V. V. Kremenetsky, S. V. Motyzhev, S. G. Poyarkov, P.-M. Poulain, S. V. Stanichny, and D. M. Soloviev (2004), Water circulation and characteristics of currents of different scales in the upper layer of the Black Sea from drifter data, *Oceanology*, *44*(1), 30–43.

R. Abarca del Rio, Departamento de Geofísica (DGEO), Universidad de Concepción, Casilla Postal 160-C, Concepción, Chile.

A. Chaigneau, LOCEAN (T45-55, 4éme etage), Université P. et M. Curie, 4 place Jussieu, 75252 Paris cedex 05, France. (alexis.chaigneau@ird.fr)

F. Colas, Institute of Geophysics and Planetary Physics (IGPP), University of California, Los Angeles, Los Angeles, CA 90095, USA.